Influence of the Phase-Locked Loop on the Design of Microgrids Formed by Diesel Generators and Grid-Forming Converters

Diana Patricia Morán-Río, Javier Roldán-Pérez, *Member, IEEE*, Milan Prodanović, *Member, IEEE*, and Aurelio García-Cerrada, *Senior Member, IEEE*

***Abstract*—In recent years, microgrids (MGs) with renewable energy sources, diesel gen-sets, and droop-controlled converters have been increasingly used to guarantee the continuity of power supply in remote areas. Renewable energy sources have been typically connected to MGs by using an electronic converter that features the two controllers: a current-control loop and a phase-locked loop (PLL). Stability issues related to the PLLs application in electrical grids have already been addressed in the literature; however, dynamic interactions in MGs caused by PLLs have not been sufficiently explored. In this article, an MG that includes a grid-feeding voltage source converter and a grid-forming device (diesel gen-set or converter) is studied. All network elements are modeled analytically and the eigenvalue and participation-factor analyses are used to analyze the interactions between the devices. It is demonstrated that MGs formed by diesel gen-sets have reduced stability limits. Also, it is shown that stability margins of MGs formed by droop-controlled converters can be improved by changing the control parameters (e.g., PLL and internal controllers bandwidths). The main findings and conclusions are summarized and presented as a practical MG design guide. Theoretical results are validated in a lab environment comprising two 15 kW converters and one 75 kW grid emulator.**

***Index Terms*—Current control, diesel generator, droop control, microgrid (MG), phase-locked loop (PLL), small-signal analysis.**

NOMENCLATURE

Variables

α	State variable of the AVR.
β	State variable of the speed governor.
i_i, v_c, i_o	Internal current, capacitor voltage, and external current of the LCL filter.
v_i	Voltage command generated for the modulation stage.
v_{pcc}	Voltage at the connection point.
ω_{PLL}	Angular frequency generated by the PLL.
γ^{dq}	State variable of current controller.
ϕ^{dq}	State variable of voltage controller.
$\tilde{P}$, $\tilde{Q}$	Filtered active and reactive power.
δ	Relative angle of the reference frame.
ω_{nd}	Droop nominal angular frequency.
ω_n	MG nominal frequency.
v_{nd}	Droop nominal voltage.
v_f	Generator field voltage.
t_e	Electric torque.
f	Injected fuel.
v_{sg}	Stator voltage.
ψ	Stator flux linkage.
ψ_f, ψ_k	Rotor flux linkages.
i_{sg}	Stator current.
i_f, i_k	Rotor currents.
ω_{sg}	Angular frequency of the generator rotor.
ω_r	ω_{sg} in pu.
t_m	Mechanical torque.
v_r	Regulated voltage.
ϵ	State variable of the PLL.
δ_{PLL}	Angle generated by the PLL.
i_l	Current absorbed by the load.

Parameters

r_a	Armature resistance per phase in pu.
r_f, r_{kd}, r_{kq}	Rotor circuit resistances in pu.
l_d, l_q	Self-inductances of stator circuits.
l_{ff}, l_{kkd}, l_{kkq}	Self-inductances of rotor circuits.
$l_{afd}, l_{akd}, l_{akq}$	Mutual inductance stator–rotor.
l_{fkd}	Mutual inductance field-damping windings.
l_{ad}, l_{aq}	Stator mutual inductances.

Constants

τ_m	Constant term of the engine time constant.
σ	Degree of increased retarding of the engine.
H	Per unit inertia constant of the shaft.
T_E	Time constant of the excitation system.
S_E	Parameter that models the saturation function of the excitation system.

Manuscript received April 6, 2021; revised July 15, 2021 and September 3, 2021; accepted November 1, 2021. Date of publication November 11, 2021; date of current version January 19, 2022. This work was supported in part by the Spanish Ministry of Science, Innovation and Universities Through the Project Microgrid-on-Chip under Grant RTC-2017-6262-3, in part by Juan De La Cierva Incorporación Program under Grant IJC2019-042342-I, in part by Iberdrola Foundation Through the Project Cooralma, and in part by the Research Programme S2018/EMT-4366 PROMINT-CAM of Madrid Government, Spain, along with the European Social Fund. The work of Diana Patricia Morán-Río was supported by a Ph.D. Collaboration Agreement Between Comillas Pontifical University and IMDEA Energy Institute. Recommended for publication by Associate Editor M. Molinas. *(Corresponding author: Diana Patricia Morán-Río.)*

Diana Patricia Morán-Río, Javier Roldán-Pérez, and Milan Prodanović are with the Electrical Systems Unit, IMDEA Energy Institute, 28935 Madrid, Spain (e-mail: diana.moran@imdea.org; javier.roldan@imdea.org; milan.prodanovic@imdea.org).

Aurelio García-Cerrada is with the Institute for Research in Technology (IIT) ICAI Engineering School, Pontifical Comillas University, 28015 Madrid, Spain (e-mail: aurelio@comillas.edu).

Color versions of one or more figures in this article are available at https://doi.org/10.1109/TPEL.2021.3127310.

Digital Object Identifier 10.1109/TPEL.2021.3127310

K_E	Self-excitation constant of the excitation system.
Control Parameters	
k_{pC}	Proportional constant of the controller C.
k_{iC}	Integral constant of the controller C.
Base values	
U_B, I_B, ω_B	Base of voltage, current, and angular frequency.
General Definition of Variables	
X_i^j	Value of variable x_i^j at the operating point.
x_i^{*j}	Set-point of the variable x_i^j
x^{dq}	Variable x is represented in the d–q axis.
x^{DQ}	Variable x is represented in the D–Q axis.

I. Introduction

THE concept of microgrid (MG) was originally introduced as an alternative solution for electricity supply in remote residential and industrial areas, and physical islands [2], [3]. These small-scale grids have been custom-made according to their specific application requirements and the availability of primary resources. In an MG, additional energy storage and generation devices (such as batteries and diesel gen-sets) may be required to guarantee the continuity of power supply [4], [5]. In islanded MGs, a simple control solution is to use a grid-forming (GFo) device to energize the network and set the MG voltage and frequency and to allow the connection of other devices operating in grid-following mode, also known as grid-feeding (GFe) mode [6], [7]. In the past, diesel gen-sets have been exclusively used as GFo devices; however, in recent years, there have been more examples of droop-controlled power converters taking over this role. The most common converter topology for GFe devices is a voltage source converter (VSC) that comprises a current controller and a phase-locked loop (PLL).

A control system based on a PLL performs correctly in stiff grids and when the network dynamics is relatively slow [7]. However, it has been demonstrated that the PLL design of a GFe-VSC (the PLL, from now on) has a strong influence on the stability of grid-tied converters and the network as the whole. The instability of a grid-connected converter may result from a negative resistance found in its dq impedance model that is related to the PLL bandwidth and the power levels injected to the grid [8]. Indeed, it has been found that the PLL bandwidth limits the maximum power transfer in high-voltage dc interconnections [9]. The interaction between the PLL and dc-voltage controller can also have a negative effect on the stability of grid-connected converters that operate as rectifiers [10]. Some recommendations on the design of current controllers, PLLs, and dc-voltage controllers for grid-connected converters were presented in [10]. Since MGs have lower inertia when compared to conventional grids, it is important to verify if PLL introduces the same stability restrictions, as well as to analyze other aspects that may compromise the converter and grid stability.

The effect of PLL-SG interactions on the stability of MGs has been previously studied in the literature [1], [11]–[14]. Katiraei *et al.* [11], [12] corroborate that the power injected by a GFe converter and the design of current controller and PLL, also in MGs, have an important influence on the stability. By using eigenvalue analysis, it was found that the AVR, the excitation, and the generator inertia affect the stability of MGs with SGs and current-controlled converters [14]. The interaction between the two aspects (loading conditions and PLL design) was studied in [1]. It was shown that loading conditions and PLL design affect the same eigenvalues and therefore loading conditions should be considered in the design of the PLL. The stability of a MG consisting of droop-controlled converters and a controllable load (interfaced by a series-shunt converter that uses PLL) was studied in [15]. In that work, it was found that the PLL has a little contribution on the oscillatory modes that mainly depend on the droop parameters. Also, interactions between the dc-voltage controller and other controllers of the VSC were studied in [16] and [17]. It was found that these interactions are more pronounced in weak grids. In particular, it was found that the stability margins are reduced when the dc-voltage controller and PLL have similar bandwidths.

PLL implementations in the conventional grids have been extensively studied [8]–[10]. The interactions of PLL with the current controller and the dc-voltage controller have also been studied in conventional grids and MGs. However, interactions between different control loops of all the connected devices such as AVR, excitation, droops, and voltage and current controllers of GFo VSCs have not been studied in detail. In addition, for the case of MGs, there are no clear guidelines for the design of the controllers, such as those already existing for VSCs connected to conventional grids. Furthermore, the models of SGs used to analyze stability commonly neglect the damping windings [14], [18], although several publications have taken them into account [11], [12]. Finally, small-signal models of such hybrid and diverse MGs have been rarely validated experimentally [12].

Therefore, according to the authors' best knowledge, the dynamic interactions caused by PLLs in MGs (formed by either diesel gen-sets or droop-controlled converters) have not been still sufficiently explored. Also, no general design rules have been proposed to assist the designer in choosing the control parameters in MGs formed of GFo and GFe devices.

This article focuses on the interaction between GFe and GFo devices in MGs. The small-signal models of MGs formed by either diesel generator or droop controller VSC are developed and used to study the influence of the GFe-PLL on the stability of the MG. The main contributions of the article are as follows.

1) Study of dynamic interactions in islanded microgrids between typical GFo elements and GFe converters.
2) The impact of GFe converters and their PLL on the stability of MG for different network scenarios is studied by using participation factors and eigenvalue analysis.
3) Detailed design guidelines are proposed to help MG designer choose and tune control parameters and guarantee the MG stability.
4) Comparison between the two most common GFo devices, namely, a diesel gen-set and a droop-controlled VSC with respect to MG stability.

Other contributions of the article are as follows.

1) Development of comprehensive small signal models of microgrids formed by, in one case, a diesel generator and, in the other, a droop-controlled VSC.
2) Experimental validation of small-signal models and stability boundaries using an experimental platform based on two 15 kW VSCs, one 75 kW grid emulator, and 30 kW loadbank.

The rest of this article is organized as follows. The MGs topology is described in Section II. Section III explains the

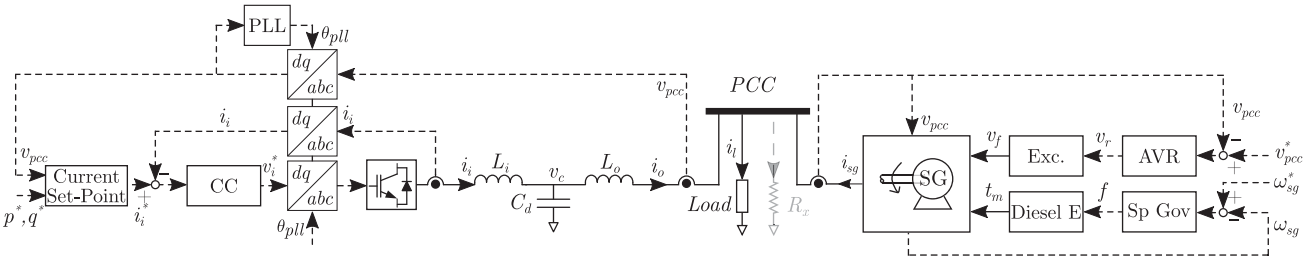

Fig. 1. Electrical and control diagram of a diesel gen-set and a GFe-VSC connected to a common bus (PCC) feeding a load [1].

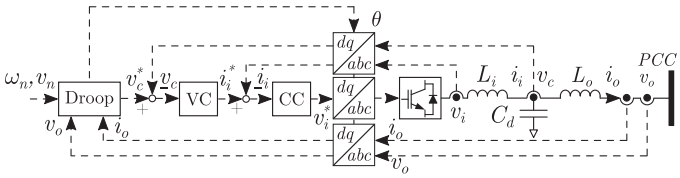

Fig. 2. Electrical and control diagram of the GFo-VSC.

small-signal model of each device and of the complete MGs. Section IV studies the interactions between the PLL and the rest of elements using eigenvalues and participation factors. The design guide is developed in Section V, while experimental results are presented and discussed in Section VI. In Section VII, results are discussed, including the effect of additional control loops and advanced synchronization algorithms. Finally, Section VIII concludes this article.

II. Application Overview

A. System Description

Fig. 1 shows the MG studied in this article. The grid can be formed either by a diesel generator (see Fig. 1, in the right) or by a droop-based converter (see Fig. 2). The MG also includes a GFe-VSC and a load. All the devices are connected to the same point of common coupling (PCC). This topology may be used for energy supply of remote residential or industrial areas [2], [3].

The diesel generator includes a diesel engine mechanically coupled to an SG that has its excitation system formed of an alternator and a diode rectifier. The PCC voltage and frequency are controlled by the AVR and the speed governor of the SG, respectively. The AVR generates the set-point for the excitation system (v_r) while the speed governor generates the set-point for the fuel injection (f).

In order for this study to be applicable to larger MGs and especially MG power parks (GFo converters all connected to the same busbar), we considered GFo-VSC with LCL filters. These filters are commonly used to interface GFo-VSC in MGs [19] or to provide the connection to the PCC. Current and voltage loops are used to control the ac capacitor voltage. Also, voltage and frequency droop controllers are used to set the MG voltage and frequency.

The GFe-VSC is connected to the PCC via an LCL filter. The active and reactive power injections are controlled indirectly by using a current controller implemented in dq. The SRF is obtained by using a PLL [7].

B. Reference Frames

The small-signal models have been developed following the methodology presented in [19]. State-space equations are represented in a common reference frame (DQ) synchronized with the output voltage of the GFo device (SG or droop-controlled VSC). An additional reference frame (dq) generated by the PLL is used to model the GFe-VSC. Variables are transformed between the reference frames by using [19]

$$\begin{bmatrix} f^D \\ f^Q \end{bmatrix} = \begin{bmatrix} \cos\delta & -\sin\delta \\ \sin\delta & \cos\delta \end{bmatrix} \begin{bmatrix} f^d \\ f^q \end{bmatrix} \tag{1}$$

where δ is the angle of the dq reference frame with respect to the DQ reference frame.

III. Small-Signal Modeling of MG Devices

The small-signal models of the diesel generator, the GFo-VSC and the GFe-VSC are introduced in this section, while their detailed models are provided in the Appendix. The notation is defined in the Nomenclature.

A. Small-Signal Model of a Diesel Generator

The gen-set model consists of the equivalent electrical circuit of the SG, the excitation circuit, the prime mover (diesel engine), the controllers mentioned above (voltage and frequency), and a shaft model [12], [18], [20]–[22]. The SG equations are presented in pu and are in the (DQ) reference frame [18].

1) Electromechanical Model: The SG is modeled by a set of differential equations with flux linkages as state variables and a set of algebraic equations that links the currents and the flux linkages [18]. A three-wire system has been considered, so o-axis equations are omitted [18]. A laminated salient-pole machine has been considered. Therefore, the small-signal model has five states, $x_\psi = [\psi_D, \psi_f, \psi_k^D, \psi_Q, \psi_k^Q]^T$ (see Nomenclature for details)

$$\begin{aligned} \Delta\dot{x}_\psi = A_{EM}\Delta x_\psi + B_{EM1}\left[\Delta v_f\right] + B_{EM2}\left[\Delta v_{sg}^{DQ}\right] \\ + B_{EM3}\left[\Delta\omega_r\right] \end{aligned} \tag{2}$$

where A_{EM}, B_{EM1}, B_{EM2}, and B_{EM3} are calculated analytically according to (43) and (48) (in the Appendix). The output variables are the electric torque, the stator currents, and the field current. Currents can be calculated from flux linkages using (38)−(42), while the electric torque is [18]

$$t_e = i_{sg}^Q\psi^D - i_{sg}^D\psi^Q. \tag{3}$$

The linearized expressions for the electric torque and the stator and field currents are

$$\left[\Delta t_e\right] = C_{EM1}\Delta x_\psi \tag{4}$$

$$\begin{bmatrix}\Delta i_{sg}^{D}\\ \Delta i_{sg}^{Q}\end{bmatrix} = C_{EM2}\Delta x_{\psi},\quad \left[\Delta i_f\right] = C_{EM3}\Delta x_{\psi}. \tag{5}$$

The analytical expressions for C_{EM1}, C_{EM2}, and C_{EM3} are shown in the Appendix, in (49)−(51).

2) Motion Equations: The shaft is modeled by using the following differential equation [18]:

$$\frac{d\omega_r}{dt} = \frac{t_m - t_e}{2H}.$$

This equation is linear and can be rewritten as [18]

$$\left[\Delta\dot{\omega}_{sg}\right] = B_{S1}\left[\Delta t_m\right] + B_{S2}\left[\Delta t_e\right]. \tag{6}$$

3) Exciter: The exciter includes an alternator in series with a diode rectifier [21]. The model AC5A has been used [23]

$$\frac{dv_f}{dt} = \frac{1}{T_E}v_r - \frac{S_E + K_E}{T_E}v_f. \tag{7}$$

This model can be linearized, yielding

$$\left[\Delta\dot{v}_f\right] = A_E\left[\Delta v_f\right] + B_{E1}\left[\Delta v_r\right] \tag{8}$$

$$\left[\Delta v_f\right] = C_E\left[\Delta v_f\right]. \tag{9}$$

4) Engine: The dynamics of the diesel engine used as prime mover is modeled as a first-order nonlinear system, as it is commonly done in the literature [20]

$$\frac{dt_m}{dt} = \frac{1}{\tau_m(\sigma + t_m)}(f - t_m). \tag{10}$$

The linearized model becomes (details in the Appendix):

$$\left[\Delta\dot{t}_m\right] = A_D\left[\Delta t_m\right] + B_D\left[\Delta f\right] \tag{11}$$

$$\left[\Delta t_m\right] = C_D\left[\Delta t_m\right]. \tag{12}$$

5) Automatic Voltage Regulator (AVR): For simplicity, a proportional–integral (PI) controller has been adopted for the AVR [20]. This regulator controls the amplitude of the PCC voltage (v_{sg}), $(v_{sg} = v_{pcc})$ by generating the set-point for the regulated voltage (v_r). The module of the PCC voltage is

$$v_{sg} = \sqrt{{v_{sg}^{D}}^2 + {v_{sg}^{Q}}^2}. \tag{13}$$

The linearized model of the AVR is (details in the Appendix)

$$\left[\Delta\dot{\alpha}\right] = B_{AVR1}\left[\Delta v_{sg}^{*}\right] + B_{AVR2}\left[\Delta v_{sg}^{DQ}\right] \tag{14}$$

$$\left[\Delta v_r\right] = C_{AVR}\left[\Delta\alpha\right] + D_{AVR1}\left[\Delta v_{sg}^{*}\right] + D_{AVR2}\left[\Delta v_{sg}^{DQ}\right]. \tag{15}$$

6) Speed Governor: The speed governor controls the SG frequency by modifying the fuel injection set-point. For simplicity, a PI controller has been used [20]. This controller is linear, so state-space matrices can be defined as

$$\left[\Delta\dot{\beta}\right] = B_{Gov}\left[\Delta\omega_r^{*}\right] + B_{Gov2}\left[\Delta\omega_r\right] \tag{16}$$

$$\left[\Delta v_r\right] = C_{Gov}\left[\Delta\beta\right] + D_{Gov}\left[\Delta\omega_r^{*}\right] + D_{Gov}\left[\Delta\omega_r\right]. \tag{17}$$

7) Diesel Generator Aggregated Small-Signal Model: The detailed models defined in the previous subsections can be merged together to form the model of the diesel generator. Input variables are transformed from real to pu values, while the output variables are transformed from pu to real values. The resulting model is

$$\left[\Delta\dot{x}_{SG}\right] = A_{SG}\left[\Delta x_{SG}\right] + B_{SG1}\left[\Delta v_{sg}^{*}\right] + B_{SG2}\left[\Delta\omega_{sg}^{*}\right] + B_{SG3}\left[\Delta v_{sg}^{DQ}\right] \tag{18}$$

$$\left[\Delta i_s^{DQ}\right] = C_{SG1}\left[\Delta x_{SG}\right],\quad \left[\Delta\omega_{sg}\right] = C_{SG2}\left[\Delta x_{SG}\right]. \tag{19}$$

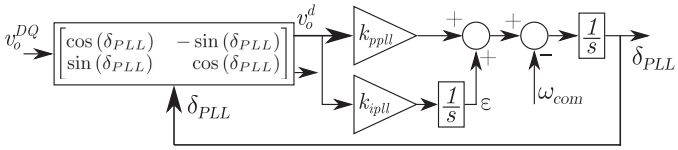

Fig. 3. SRF-PLL diagram of control in (dq).

B. Small-Signal Model of the GFe-VSC

This section presents the small-signal model for the GFe-VSC [24]. It includes an LCL filter, a current controller (in dq), the calculation of the current set-points, and a PLL. The detailed state-space model can be found in the Appendix and in the literature [24]. Only the PLL is presented here.

1) Phase-Locked Loop (PLL): A PLL is used to synchronize the GFe-VSC (in dq) with the voltage of the PCC (in DQ), as shown in Fig. 3. A typical PLL implementation has been considered [7], [24]

$$\dot{\epsilon} = k_{ipll}(v_{pcc}^{D}\cos\delta_{PLL} + v_{pcc}^{Q}\sin\delta_{PLL}) \tag{20}$$

$$\dot{\delta}_{PLL} = \epsilon + k_{ppll}(v_{pcc}^{D}\cos\delta_{PLL} + v_{pcc}^{Q}\sin\delta_{PLL}) - \omega_{sg}. \tag{21}$$

Clearly, the PLL is a nonlinear system as it has trigonometric functions involved. The linearized model is

$$\begin{bmatrix}\Delta\dot{\epsilon}\\ \Delta\dot{\delta}_{PLL}\end{bmatrix}_i = A_{PLL}^{i}\begin{bmatrix}\Delta\epsilon\\ \Delta\delta_{PLL}\end{bmatrix}_i + B_{PLL1}^{i}\left[\Delta v_{pcc}^{DQ}\right]_i + B_{PLL2}^{i}\left[\Delta\omega_{com}\right]_i. \tag{22}$$

The detailed matrices can be found in the Appendix.

2) Aggregated Small-Signal Model of a GFe-VSC: The small-signal models of the current set-points calculation, the current controller, the LCL filter, and the PLL are then combined to obtain the GFe-VSC model

$$\left[\Delta\dot{x}_{inv}\right]_{GFe} = A^{GFe}\left[\Delta x_{inv}\right]_{GFe} + B_{PQ}^{GFe}\begin{bmatrix}\Delta p^{*}\\ \Delta q^{*}\end{bmatrix}_{GFe} + B_{V}^{GFe}\left[\Delta v_{pcc}^{DQ}\right]_{GFe} + B_{\omega}^{GFe}\left[\Delta\omega_{com}\right]_{GFe} \tag{23}$$

where

$$\left[\Delta x_{inv}\right]_{GFe} = \left[\Delta\epsilon, \Delta\delta_{PLL}, \Delta\gamma^{dq}, \Delta i_i^{dq}, \Delta v_c^{dq}, \Delta i_o^{dq}\right]_{GFe}^{T}$$

$$\left[\Delta u_{inv}\right]_{GFe} = \left[\Delta p^{*}, \Delta q^{*}, \Delta v_{pcc}^{DQ}, \Delta\omega_{com}\right]_{GFe}^{T}$$

$$\left[\Delta i_{DQ}\right]_{GFe} = C^{GFe}\left[\Delta x_{inv}\right]_{GFe}.$$

One should notice v_{pcc}^{DQ} represents an input variable of the state-space model. However, in the GFe-VSC model, variables are referenced to the local dq reference frame. Therefore, they should be transformed by taking into account (105), (107), and (108), derived from (1). This transformation is directly included in the state-space matrices A^{GFe}, B_{PQ}^{GFe}, B_{V}^{GFe}, B_{ω}^{GFe}, and C^{GFe}, in (109)−(114).

C. Small-Signal Model of the GFo-VSC

The model of the GFo-VSC consists of the models of the LCL filter, the current controller, the voltage controller, and the droop controller (details in the Appendix) [19].

1) Aggregated Small-Signal Model of the GFo-VSC: All the models mentioned above are combined to obtain the small-signal model of the GFo-VSC

$$\left[\Delta\dot{x}_{inv}\right]_{GFo} = A^{GFo}\left[\Delta x_{inv}\right]_{GFo} + B_{In}^{GFo}\begin{bmatrix}\Delta\omega_{nd}\\ \Delta v_{nd}^{dq}\end{bmatrix}_{GFo} + B_{V}^{GFo}\left[\Delta v_{pcc}^{DQ}\right]_{GFo} + B_{\omega com}^{GFo}\left[\Delta\omega_{com}\right]_{GFo} \tag{24}$$

$$\left[\Delta i_o^{DQ}\right]_{GFo} = C_I^{GFo}\left[\Delta x_{inv}\right]_{GFo} \tag{25}$$

$$\left[\Delta\omega_{com}\right]_{GFo} = C_{\omega}^{GFo}\left[\Delta x_{inv}\right]_{GFo} + D_{\omega}^{GFo}\begin{bmatrix}\Delta\omega_{nd}\\ \Delta v_{nd}^{dq}\end{bmatrix}_{GFo} \tag{26}$$

where

$$\left[\Delta x_{inv}\right]_{GFo} = \left[\Delta\delta, \Delta\tilde{P}, \Delta\tilde{Q}, \Delta\phi^{dq}, \Delta\gamma^{dq}, \Delta i_i^{dq}, \Delta v_c^{dq}, \Delta i_o^{dq}\right]_{GFo}^{T}.$$

As in (23), the state-space matrices include the transformations between the reference frames (details in the Appendix).

D. Load Modeling

A resistive–inductive linear load has been considered [18]

$$\left[\Delta\dot{i}_l^{DQ}\right] = A_L\left[\Delta i_l^{DQ}\right] + B_{L1}\left[\Delta v_{pcc}^{DQ}\right] + B_{L2}\left[\Delta\omega_{com}\right]. \tag{27}$$

The state matrices can be found in the Appendix.

E. Coupling of Devices

The linearized mathematical models of the diesel gen-set, the converters, and the load include the variable Δv_{pcc}^{DQ} as an input and the current as an output. Therefore, an auxiliary resistor has been used to define this voltage adequately (R_x in Fig. 1) [19]

$$\left[\Delta v_{pcc}^{DQ}\right] = D_{R1}\left[\Delta i_o^{DQ}\right]_{GFo} + D_{R1}\left[\Delta i_o^{DQ}\right]_{GFe} + D_{R2}\left[\Delta i_l^{DQ}\right]. \tag{28}$$

F. Aggregated Model of MG1: Gen-Set, GFe-VSC, and Load

Because of the MG topology v_{pcc}^{DQ} and ω_{com} are equivalent to v_{sg}^{DQ} and ω_{sg} (their real values). Then, the MG model is

$$\begin{bmatrix}\Delta\dot{x}_{SG}\\ \Delta\dot{x}_{inv}\\ \Delta\dot{x}_L\end{bmatrix} = A^{MG1}\begin{bmatrix}\Delta x_{SG}\\ \Delta x_{inv}\\ \Delta x_L\end{bmatrix} + B_v^{MG1}\left[\Delta v_{sg}^{*}\right] + B_{\omega}^{MG1}\left[\Delta\omega_{sg}^{*}\right] + B_{PQ}^{MG1}\begin{bmatrix}\Delta p^{*}\\ \Delta q^{*}\end{bmatrix} \tag{29}$$

where

$$B_v^{MG1} = \begin{bmatrix}B_{SG1}\\ 0\\ 0\end{bmatrix}, B_{\omega}^{MG1} = \begin{bmatrix}B_{SG2}\\ 0\\ 0\end{bmatrix}, B_{PQ}^{MG1} = \begin{bmatrix}0\\ B_{PQ}^{GFe}\\ 0\end{bmatrix}.$$

G. Aggregated Model of MG2: GFo-VSC, GFe-VSC, and Load

In MG2, $v_o^{DQ} = v_{pcc}^{DQ}$. By using a virtual resistor to combine all the elements, the following model is obtained:

$$\begin{bmatrix}\Delta\dot{x}_{invGFo}\\ \Delta\dot{x}_{invGFe}\\ \Delta\dot{x}_L\end{bmatrix} = A^{MG2}\begin{bmatrix}\Delta x_{invGFo}\\ \Delta x_{invGFe}\\ \Delta x_L\end{bmatrix} + B_{\omega v}^{MG2}\begin{bmatrix}\Delta\omega_{nd}\\ \Delta v_{nd}^{dq}\end{bmatrix} + B_{PQ}^{MG2}\begin{bmatrix}\Delta p^{*}\\ \Delta q^{*}\end{bmatrix} \tag{30}$$

where

$$B_{\omega v}^{MG2} = \begin{bmatrix}B_{In}^{GFo} + B_{\omega com}^{GFo}\left[D_{P\omega}^{GFo}\ 0\right]\\ B_{\omega}^{GFe}\left[D_{P\omega}^{GFo}\ 0\right]\\ B_{L2}\left[D_{P\omega}^{GFo}\ 0\right]\end{bmatrix}, B_{PQ}^{MG2} = \begin{bmatrix}0\\ B_{PQ}^{GFe}\\ 0\end{bmatrix}.$$

IV. Analytic Study

In this section, MG1 and MG2 are analyzed. System stability is analyzed based on the information obtained from the system eigenvalues and the participation factors (Figs. 4 and 5 for MG1, and Figs. 6 and 7 for MG2, respectively) [18]. The small signal model of each scenario presented in the article was developed considering their individual operating points. The operating point of each scenario was calculated by means of a nonlinear model developed in Simulink. Then, the small signal model was used to calculate eigenvalues and participation factors. Participation factors have been calculated as [18]

$$p_{ki} = \frac{\delta\lambda_i}{\delta a_{kk}} = \psi_{ik}\phi_{ki} \tag{31}$$

where ψ_{ik} and ϕ_{ki} represent the k element of the left and right i eigenvectors, respectively. Eigenvectors were normalized so that $\psi_i\phi_i = 1$. This implies that the sum of the participation factors along a row or a column is equal to one

$$\sum_{i=1}^{n} p_{ki} = 1, \quad \sum_{k=1}^{n} p_{ki} = 1. \tag{32}$$

A. Test System Description

The nominal power of the SG is 60 kVA. The electromechanical parameters of the SG and the diesel engine are taken from [20]. For the excitation system, the reference values are taken from the AC5A model in [23]. GFo- and GFe-VSC parameters

$$A^{MG1} = \begin{bmatrix} A_{SG} + B_{SG3}D_{R1}C_{SG1} & B_{SG3}D_{R1}C^{GFe} & B_{SG3}D_{R2} \\ B_{\omega}^{GFe}C_{SG2} + B_V^{GFe}D_{R1}C_{SG1} & A^{GFe} + B_V^{GFe}D_{R1}C^{GFe} & B_V D_{R2} \\ B_{L2}C_{SG2} + B_{L1}D_{R1}C_{SG1} & B_{L1}D_{R1}C^{GFe} & A_L + B_{L1}D_{R2} \end{bmatrix}$$

$$A^{MG2} = \begin{bmatrix} A^{GFo} + B_{\omega com}^{GFo}C_{\omega com}^{GFo} + B_V^{GFo}D_{R1}C_I^{GFo} & B_V^{GFo}D_{R1}C^{GFe} & B_V^{GFo}D_{R1}C_L \\ B_{\omega}^{GFe}C_{\omega}^{GFo} + B_V^{GFe}D_{R1}C^{GFe} & A^{GFe} + B_V^{GFe}D_{R1}C^{GFe} & B_V^{GFe}D_{R2}C_L \\ B_{L2}C_{\omega}^{GFo} + B_{L1}D_{R1}C_I^{GFo} & B_{L1}D_{R1}C^{GFe} & A_L + B_{L1}D_{R2}C_L \end{bmatrix}$$

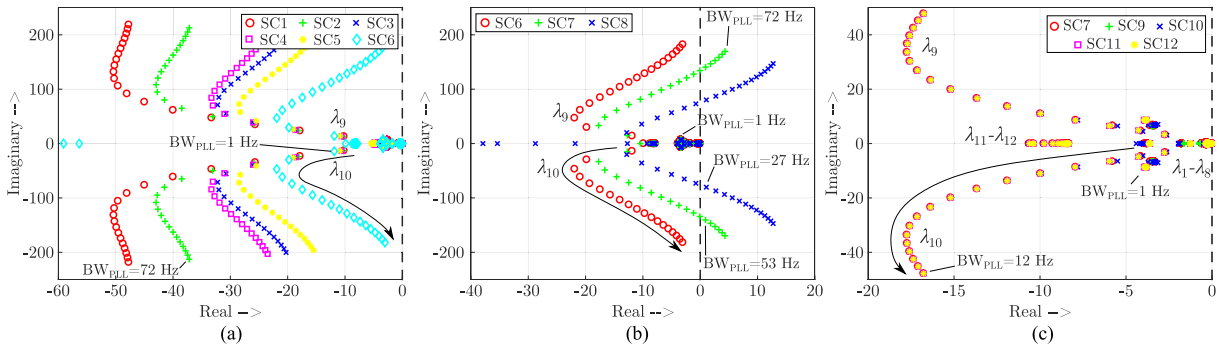

Fig. 4. Trajectory of MG1 eigenvalues (low frequency) for different scenarios when the bandwidth of PLL is increased. (a) GFe-VSC injecting 22%, 33%, and 50% of the load, which takes two values (12 and 18 kW). (b) Current controller bandwidths of GFe-VSC: 490, 380, and 260 Hz. (c) Different designs of speed governor and SG inertia. See Table III for detailed definition of scenarios.

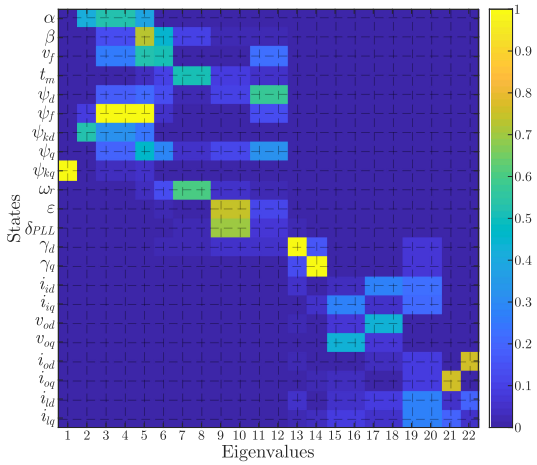

Fig. 5. Participation matrix for MG1, SC1. Eigenvalues are ordered left to right according to their distance from the imaginary axis.

TABLE I
DIESEL GENSET PARAMETERS (SC1)

Par.	Val.	Par.	Val.	Par.	Val.
r_a	$3.54E{-}2$	l_{kkq}	1.4967	σ	1
r_f	$6E{-}4$	l_{ad}	2.38	k_{pAVR}	2.47
r_{kd}	$3.54E{-}2$	l_{aq}	1.24	k_{iAVR}	0.42
r_{kQ}	$4.28E{-}2$	H	$3.704E{-}1$	k_{pGov}	5.57
l_d	2.83	T_E	0.8	k_{iGov}	6.39
l_q	1.69	S_E	1	Poles	4
l_{ff}	2.6371	K_E	0.68	U_B	$400\sqrt{2}$
l_{kkd}	2.58	τ_m	0.1	f_B	50Hz

are defined in Table II. Two VSCs of the same power rating (15 kVA) (and, therefore, the same LCL parameters) have been considered, because the converter power ratio introduces a key restriction during the PLL design.

A base scenario (SC1) has been defined for both MGs. In SC1, the load is consuming 18 kW. The active power set-point for the GFe-VSC is 4 kW and the reactive power set-point is zero. The voltage and frequency set-points of the SG are 400 V and 50 Hz, respectively. The AVR and the speed governor have been designed to be as fast as possible, resulting in bandwidths of

TABLE II
GFO AND GFE-VSC PARAMETERS (SC1)

Param	Val	Param	Val
L_i	2.3 mH	$k_{iv}(GFo)$	6.92
R_i	72.2 mΩ	m_p	6.67E-6
L_o	0.93 mH	n_q	3.33E-4
R_o	29.2 mΩ	ω_c	31.41
C_d	8.83 μF	$k_{pc}(GFe)$	4.43
$k_{pc}(GFo)$	1.81	$k_{ic}(GFe)$	3.05E3
$k_{ic}(GFo)$	2.17E3	k_{ppll}	0.0136
$k_{pv}(GFo)$	0.0553	k_{ipll}	0.0492

0.17 and 1.7 Hz, respectively (see Table I). Controllers have been designed by using open-loop techniques, with phase margins of 45° (speed governor and current controllers), 50° (AVR), and 60° (PLL and voltage controller). The bandwidth of the current controller and the PLL of the GFe-VSC are set to 490 and 1.4 Hz, respectively, while the bandwidth of the current and voltage controllers of the GFo-VSC are set to 490 and 30 Hz, respectively. The rest of the parameters are defined according to Table II. The additional scenarios considered in the article are defined in Table III. Scenarios SC2–SC23 are derived by modifying some parameters of a base scenario.

B. Participation Factors for MG1 (Diesel Gen-Set)

Fig. 5 shows the modulus of the participation factors for MG1, SC1. For instance, the modulus of the participation factors of state δ_{PLL} in Modes 7–13 are 0.03, 0.03, 0.7, 0.7 0.08, 0.08, and 0.03, respectively. Modes are ordered by numbers in the x-axis according to their proximity to the imaginary axis (left meaning closer to it). The states related to the SG are mainly affected by Modes $1-5$. These modes have limited influence on the the PLL states, while their influence on the rest of the GFe states is negligible. Modes $6-12$ participate in the engine and the rotor states (ω_r and t_m), but also in the PLL states (ϵ and δ_{PLL}), thus creating a dynamic interaction between the two devices. Modes 12 and 13 are related to the PLL and the current controller and, therefore, represent their interaction. The rest of the modes are mainly related to electromagnetic phenomena and represent the

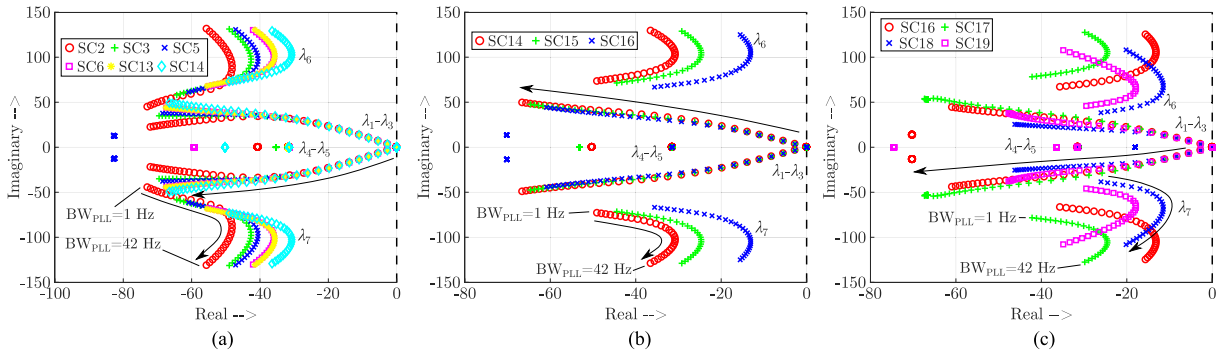

Fig. 6. Trajectory of low-frequency eigenvalues of MG2 for different scenarios when the bandwidth of PLL is increased. (a) GFe-VSC injecting 33%, 50%, and 67% of power load that takes two values (12 and 18 kW). (b) GFe-VSC current controller bandwidths: 490, 380, and 260 Hz. (c) Different designs of the GFo-VSC voltage and current controllers. See Table III for detailed definition of scenarios.

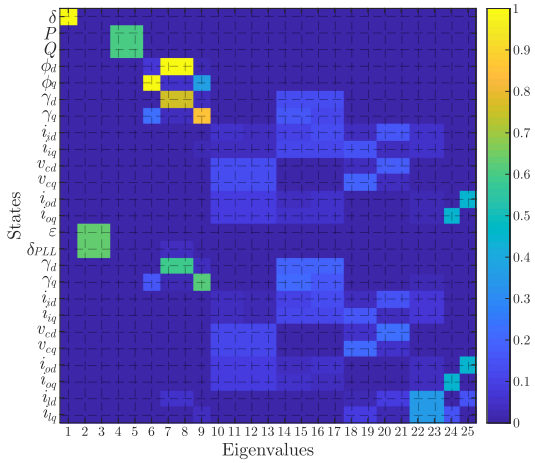

Fig. 7. Participation matrix of MG2, SC1. Eigenvalues are ordered left to right according to their distance from the imaginary axis.

link between the current controller, the LCL filter variables, and the load.

The interaction between δ_{PLL} and the mechanical states is stronger especially for the reduced bandwidth of the speed governor loop. Additionally, the states ω_r, t_m, and γ_d show a stronger coupling with δ_{PLL} when the bandwidths of the PLL and the current controller decrease, and also when the inertia of the generator is reduced. The states δ_{PLL} and γ_d also show a stronger interaction when the power injected by the GFe-VSC increases. No relevant interactions were observed between the PLL and the voltage controller of the diesel gen-set, as it was previously reported in the literature when standard excitation AC4A was used [14], [23]. This could be motivated by the use of different AVR and excitation system [25].

From these results, it is clear that the PLL participates in the mechanical states of the MG. This will be studied in the next section where the system eigenvalues will be analyzed.

C. Stability Limits of MG1 (Diesel Gen-Set)

Fig. 4 shows how the eigenvalues of MG1 are affected by the PLL bandwidth in various scenarios. Only low-frequency eigenvalues are shown because PLL mainly affects low-frequency dynamics. Fig. 4(a) considers six different loading scenarios (SC1–SC6), with three different levels of power injected by GFe-VSC (22%, 33%, and 50% of load). The eigenvalues that are more affected by the PLL move toward the imaginary axis when the relative power share of the GFe-VSC increases. This effect is more pronounced and evident at light load conditions. For instance, in both SC1 and SC4, Gfe-VSC has a 22% power share but the eigenvalues in SC4 are located closer to the imaginary axis. This will result in a reduction of the stability limits linked with the parameters of the PLL.

TABLE III
DEFINITION OF SCENARIOS SC2–SC23 SHOWING THE INITIAL (BASE) SCENARIO, THE PARAMETER CHANGED, AND ITS NEW VALUE

SC	Base SC	Changed Param	New Value
SC2	SC1	P_{GFe}	6 kW
SC3	SC1	P_{GFe}	9 kW
SC4	SC1	P_{GFe}; P_L	2,6 kW; 12 kW
SC5	SC1	P_{GFe}; P_L	4 kW; 12 kW
SC6	SC1	P_{GFe}; P_L	6 kW; 12 kW
SC7	SC6	$BWGFe_{cc}$	380 Hz
SC8	SC6	$BWGFe_{cc}$	260 Hz
SC9	SC7	J	3,6 kg m^2
SC10	SC7	J	0,9 kg m^2
SC11	SC7	BWf	2,1 Hz
SC12	SC7	BWf	0,5 Hz
SC13	SC1	P_{GFe}; P_L	12 kW; 18 kW
SC14	SC1	P_{GFe}; P_L	8 kW; 12 kW
SC15	SC14	$BWGFe_{cc}$	380 Hz
SC16	SC14	$BWGFe_{cc}$	260 Hz
SC17	SC16	GFo_{vc}; GFo_{cc}	31 Hz; 260 Hz
SC18	SC16	GFo_{vc}; GFo_{cc}	20 Hz; 490 Hz
SC19	SC16	GFo_{vc}; GFo_{cc}	20 Hz; 260 Hz
SC20	SC1	P_{GFe}; P_L; GFe_{cc}; GFe_{PLL}	9 kW; 23 kW; 120 Hz; 17 Hz
SC21	SC1	P_{GFe}; P_L; GFo_{cc}; GFo_{vc}; GFe_{cc}; GFe_{PLL}	11 kW; 13 kW; 520 Hz; 34 Hz; 250 Hz; 19 Hz
SC22	SC20	GFe_{cc}; GFe_{PLL}	380 Hz; 7 Hz
SC23	SC21	GFo_{cc}; GFo_{vc}; GFe_{cc}; GFe_{PLL}	380 Hz; 40 Hz; 380 Hz; 7 Hz

TABLE IV
CHANGES THAT REDUCE PLL BANDWIDTH STABILITY LIMITS

Parameter	Type of change in parameter
P_L	Decrease ↓
P_{GFe}/P_{GFo}	Increase ↑ (specially in MGs with SG)
$BWGFe_{cc}$	Decrease ↓
$BWGFo_{vc}$	Decrease ↓
$BWGFo_{cc}$	Increase ↑

In Fig. 4(b), three scenarios with different bandwidths of the current controller are studied (SC6, SC7, and SC8). The current controller bandwidth has a strong influence on the maximum bandwidth achievable by the PLL. For instance, for a current controller bandwidth of 260 Hz (SC8), the MG becomes unstable when the PLL bandwidth is higher than 27 Hz.

Different scenarios for the inertia and the design of the speed governor have been examined and the results are shown in Fig. 4(c) (SC7, SC9, SC10, SC11, and SC12). It shows that the SG inertia and the bandwidth of the speed governor have little influence on the eigenvalues linked with PLL. This interaction is even weaker when the PLL bandwidth increases.

Summarizing, for the type of generator, prime movers, and controllers considered, the mechanical parameters have only a small contribution to the eigenvalues related to the PLL. In contrast, the loading conditions and the design of the current controller greatly affect the aforementioned eigenvalues. With this respect, high levels of load, low relative power contribution from the GFe-VSC, and fast current controllers are preferable. A summary is presented in Table IV.

D. Participation Factors for MG2 (GFo-VSC)

Fig. 7 shows the participation matrix for MG2 for SC1. All the modes of MG2 mainly participate in one state (or in a couple of related states, like ϵ and δ_{PLL}). Clearly, the states and modes are more decoupled than in MG1. It can be seen that Modes $2-3$ mainly participate in the states related to the PLL, and to a lesser extent, to the voltage controller of the GFo-VSC. The interaction between these parameters is studied in the following section.

E. Stability Limits of MG2 (GFo-VSC)

Fig. 6 shows the trajectory of the low-frequency eigenvalues of MG2 for the increase of the PLL bandwidth, for different scenarios. Fig. 6(a) shows that in MG2, as it happened in MG1, the eigenvalues move to the right when the power injected by the GFe-VSC increases. Scenarios with light load conditions (SC5, SC6, and SC14) also tend to destabilize the system compared to those with more load (SC2, SC63, and SC13, respectively).

Fig. 6(b) shows that eigenvalues move toward the imaginary axis if the bandwidth of the current controller decreases, as it happened in MG1. This may result on limited PLL bandwidth for some loading conditions.

Fig. 6(c) shows MG2 eigenvalues when the bandwidth of the PLL increases for different designs of the GFo-VSC voltage and current controllers. As shown in Fig. 6(c), the eigenvalues are closer to the imaginary axis when the voltage controller is slowed down (SC18 and SC19). In general, interactions between the voltage and current controllers are avoided by ensuring a sufficient time-constant separation between them. More precisely, current controllers are typically designed to be faster than voltage controllers. However, as shown in Fig. 6(c), increasing the current controller bandwidth has a negative effect on the stability (SC18), unless the voltage controller bandwidth is increased at the same time (SC16).

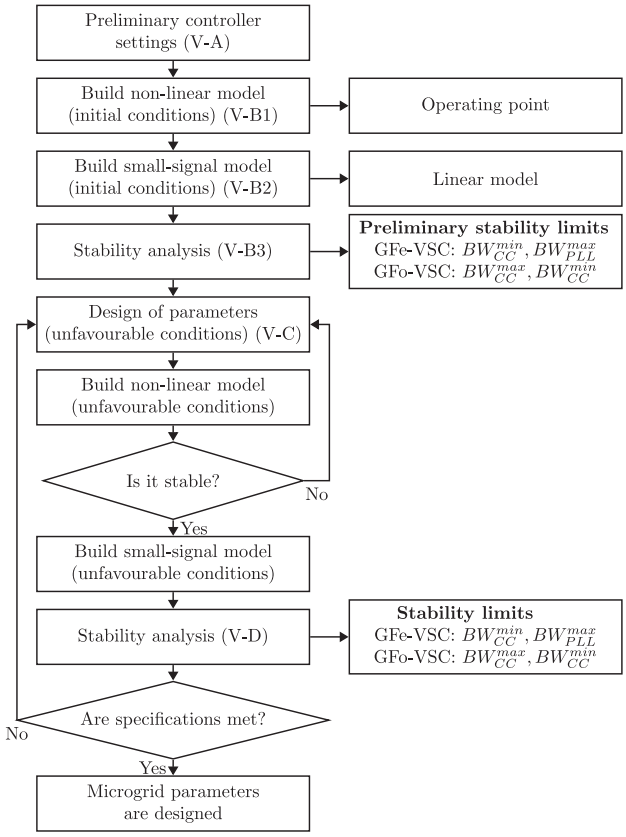

Fig. 8. Flowchart of the proposed method for the design of MG controllers.

Summarizing, loading conditions and the design of the GFe-VSC current controller have impact on the eigenvalues related to the PLL, just as it happened in MG1. High-load, low relative power injection by the GFe-VSC and fast current controller for the GFe-VSC allow higher PLL bandwidths. The GFo-VSC also affects the PLL design. The PLL bandwidth can be increased with fast voltage controllers and slow current controllers. In this case, the loading conditions do not limit the PLL design as much as in the case of MG1. These aspects are summarized in Table IV.

V. GUIDELINES FOR THE DESIGN OF CONTROL PARAMETERS IN AN MG

The conclusions drawn from the analysis have been used to develop and propose design guidelines for the selection of control parameters in an MG. The guidelines assume the use of the small-signal model; however, some of the recommendations are generally applicable and are helpful even without the model. The flowchart with the design procedure is shown in Fig. 8. The boxes of the flowchart also indicate the section in which the task is addressed. The design of the parameters is based on the stability limits calculated using the small-signal model.

Initially, a stable scenario is used by applying typical values for the controllers. Preliminary stability limits are calculated by assuming this scenario, that is also used to compute a stable operating point. Then, the preliminary stability limits are used to define the controllers of the MG under most unfavorable conditions for the stability (low levels of power injected by the GFo device and high levels of power injected by the GFe-VSC). Both nonlinear and linear models are developed for the unfavorable condition scenario. MG controllers are redesigned to meet the specifications, taking into account the stability limits under the unfavorable conditions.

A. Preliminary Controller Settings

1) Diesel-Based MGs: To start with, the controllers of diesel gen-sets can be configured to be as fast as it is required while the bandwidth of the PLL should be similar to that of the frequency controller. The current controller of the GFe-VSC should be designed in a typical way by using the desired settling time and the adequate damping of the LCL filter resonance [6], [7]. The bandwidth of the dc-voltage controller should not be close to that one used for the PLL to avoid undesired oscillations. Also, it should not be unnecessarily wide [16], [26].

2) Converter-Based MGs: The current controllers of the GFe-VSC and the GFo-VSC should be designed by using standard design rules [6], [7]. Then, the voltage controller of the GFo-VSC should be configured to be as fast as possible, yet it needs to guarantee a sufficient time-constant separation between the current and the voltage loops. The PLL can be designed to be fast enough to track standard frequency variations in power grids [27] (a bandwidth between 1 and 10 Hz would work in most cases). The dc-voltage controller, if required, should be designed in a similar way to the case of diesel-based MGs.

B. Model Development, Operating Points, and Stability

1) Nonlinear Model and Operating Point: A nonlinear model of the microgrid is used to perform the time-domain simulations and to calculate the operating point. The model should include all the nonlinear equations of the desired GFo device (SG or VSC), the GFe, and the load. In order to find a suitable operating condition to start the analysis and the control design, it is recommended to set the GFo to feed a moderate load (50%–80% of its rated power) and the GFe not to inject any power.

2) Small-Signal Model of the MG: A small-signal model of the MG should be developed. It can be obtained by using the analytical expressions included in this article (in Section III), or by using automatic tools (e.g., Simulink Control Design toolbox [28]).

3) Initial Conditions for the Stability Test: Stability limits of the bandwidth of MG controllers can be found by using the small-signal analysis techniques presented in the article. These limits will be used for the design of MG parameters under most unfavorable conditions.

C. Fine-Tuning of Control Parameters Under Unfavorable Conditions

An unfavorable operating condition can be found when the GFo injects its minimum power and when the GFe relative power injection is high. By following the steps mentioned before, the designer may have already found control parameter values that guarantee the stability. However, a more elaborated selection can lead to improved stability margins and an optimization procedure can be used to find the optimal selection.

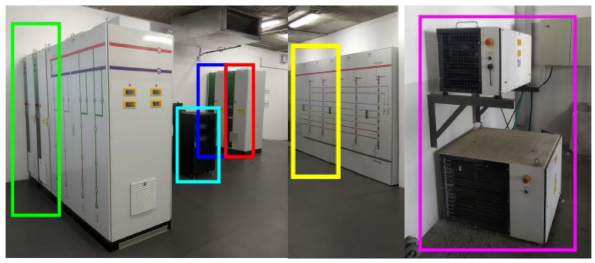

Fig. 9. Lab photograph. From left to right: (green) 75 kVA converter used as emulator for the SG and part of the load in MG1, (cyan) real-time targets (converter controllers), (blue) 15 kVA converter used as GFo-VSC, (red) 15 kVA converter used as GFe-VSC, (yellow) ac bus bars and (magenta) loads.

1) MGs Formed by Diesel Gen-Sets: The PLL can be redesigned by taking into account the upper limit of its bandwidth and the expected frequency variations. If the design specifications cannot be met, the GFe-VSC current controller should be made faster to increase the stability limit of the PLL bandwidth.

2) MGs Formed by GFo-VSCs: The GFe-VSC current controller can be redesigned by taking into account the lower stability limit imposed by the MG and other restrictions imposed by the LCL resonance and the switching frequency. Finally, the PLL can be redesigned by taking into account its upper stability limit and the expected variations of the MG frequency. If the design specifications cannot be fulfilled, the voltage and current controllers should be redesigned by reducing the bandwidth of the GFo-VSC current controller and increasing both the bandwidth of the GFe-VSC current controller and the bandwidth of the voltage controller of the GFo-VSC to allow for wider PLL bandwidths.

D. Stability Analysis Under Unfavorable Conditions

It is recommended to calculate the small-signal model for the operation under these conditions. Also, it is recommended to carry out transient simulations in order to check if the system operates within its limits even during large transients. If the system is not well damped (e.g., damping factor smaller than 0.3), the controllers should be redesigned. This can be checked by analyzing the system eigenvalues. For example, the PLL and the current controller of the GFo-VSC can be slowed down, while the speed of the current controller of the GFe-VSC and the voltage controller of the GFo-VSC can be increased.

VI. Experimental Validation

A. Prototype Description

MG1 and MG2 were implemented in the Smart Energy Integration Lab (SEIL) [29], [30] (Figs. 9 and 10). A 75-kVA VSC was used as the grid emulator. It used model-based approach to emulate the operation of the diesel gen-set and part of the load (12 kW) in MG1. Two 15-kVA converters were used as

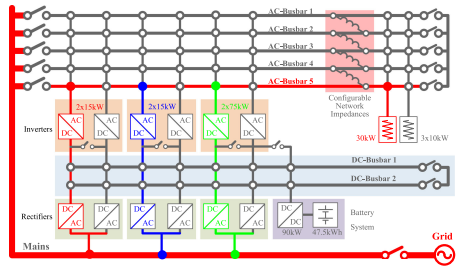

Fig. 10. Electrical diagram of the laboratory. The common elements of MG1 and MG2 are shown in red (GFe-VSC and load). Grid emulator is shown in green, and GFo-VSC is shown in blue. MG1: red and green. MG2: red and blue.

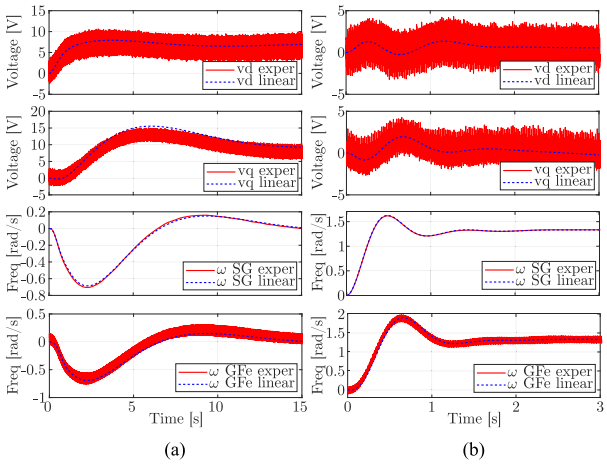

Fig. 11. Response of MG1 when there is step change of (a) 10 V and (b) 0.2 Hz in the SG voltage and frequency set-points. (Red) Experimental and (blue) linearized model results.

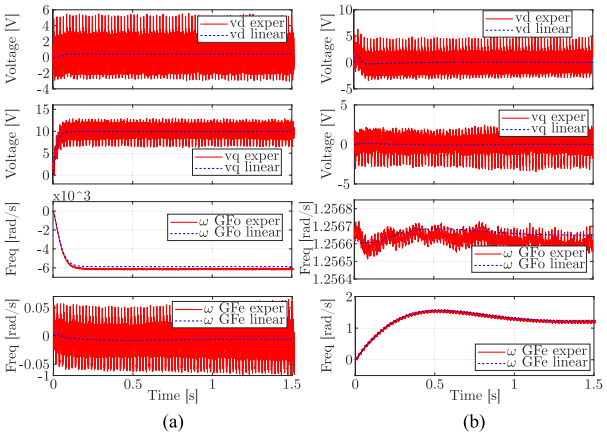

Fig. 12. Response of MG2 for (a) step of 10 V applied to the nominal voltage of the droop controller and (b) step of 0.2 Hz applied to the nominal frequency of the controller. (Red) Experimental results and (blue) linearized model results.

GFo-VSC and GFe-VSC in the experimental validation. Different loading conditions were implemented by using a variable, progammable resistive load bank. The single-line electrical diagrams of the two MG implementations are shown in Fig. 10 (MG1 in red and green and MG2 in red and blue).

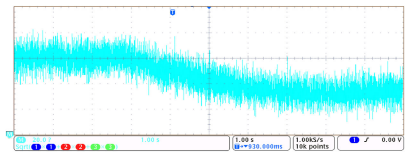

Fig. 13. Response of modulus of v_{abc}, when there is a 10-V step change of the SG set-point. Horizontal scale: 1 s/div; vertical scale: 20 V/div.

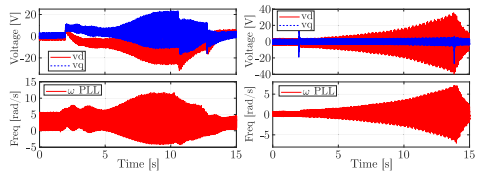

Fig. 14. Response of MG1 in SC20 (a) and MG2 in SC21 (b) when the load decreases 1 kW (and hence the ratio of power injected by the GFe-VSC increases) making both MGs unstable.

B. Validation of Small-Signal Models

Figs. 11 and 12 show a comparison between the transient responses obtained from the experimental setup and the linearized models when applying SC1. Since MG dynamics is slow, the models are validated by using dq signals, as it is common in the literature [19], [24]. Experimental dq signals were obtained from the control boards of the converters, without filters. The experimental results were also obtained by using an oscilloscope, as shown in Fig. 13. However, in this case, it was difficult to compare the theoretical results with the experimental waveforms. A 10-V and a 0.2-Hz step were applied to the set points of the SG voltage and frequency controllers (see Fig. 11). The same steps were used for the GFo-VSC (see Fig. 12). Clearly, the small-signal models accurately reproduce the low-frequency dynamics of the experimental platform. Since high-frequency phenomena (e.g. pulsewidth modulation) was not considered in the modeling, high-frequency dynamics cannot be predicted by using the developed linear models. In v_{dq}, ω_{GFe}, and ω_{GFo}, some harmonics can be observed due to the lack of filters at the measuring stage. This oscillations are not present in ω_{SG} because this variable is taken from the emulated model.

C. Validation of Stability Limits

The theoretical stability limits of the PLL were validated experimentally. MG1 was validated for SC20, where the load was 23 kW (12 kW were emulated). The GFe-VSC injected 9 kW (39%). The SG parameters are defined in Table I. The current controller bandwidth was 120 Hz. In this scenario, the linear model analyses suggested a maximum PLL bandwidth of 18 Hz. However, during the validation, the system remained stable up to a bandwidth of 17 Hz. Even though the dynamics was accurately described by the linear model, the range of frequency for the system to be marginally stable differs slightly. This is common in experimental validations as linear models show different sensitivity to parameter variation at the edge of the stability region [31]. However, small-signal tools are still useful in grid applications since the main objective here is to ensure that the system operates away from the unstable region [18]. Fig. 14(a) shows the response of MG1 when the PLL bandwidth was 17 Hz

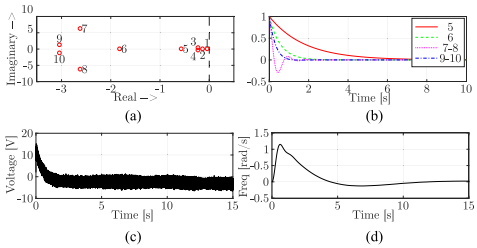

Fig. 15. Response of MG1 in SC22 when the load decreased 1 kW with a recommended controller design. Comparison between the time responses obtained from the corresponding eigenvalues and the experimental setup. (a) MG1 low frequency eigenvalues. (b) Time response of eigenvalues 5 to 10. (c) Vd step response. (d) Frequency step response.

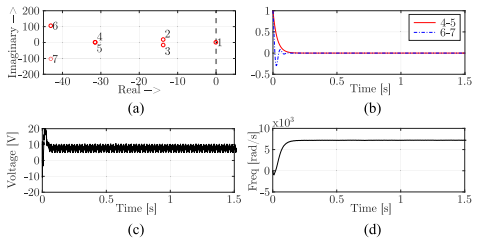

Fig. 16. Response of MG2 in SC23 when the load decreased 1 kW, with the fine-tuning. Comparison between the time responses obtained from the corresponding eigenvalues and the experimental setup. (a) MG2 low frequency eigenvalues. (b) Time response of eigenvalues 4 to 7. (c) Vq step response. (d) Frequency step response.

and a variation of the load from 23 (SC20) to 22 kW was applied. This means that the GFe-VSC power varies from 39% to 40% of the total demand. The MG becomes unstable due to the higher ratio of power injected by the GFe-VSC. At $t = 10$ s and $t = 12$ s, the load is increased again and the MG slowly recovers its stable operation. The stability limits of MG2 were validated in SC21: $P_{load} = 13$ kW, $P_{GFe-\text{VSC}} = 11$ kW, $\text{BW}_{cc\text{GFo}} = 520$ Hz, $\text{BW}_{vc\text{GFo}} = 34$ Hz, and $\text{BW}_{cc\text{GFe}} = 250$ Hz. The linear model analysis suggests the MG becomes unstable for PLL bandwidths higher than 21 Hz. In the validation, the maximum bandwidth was 19 Hz. Fig. 14(b) shows the response of MG2 in SC21 when there was a load variation from 13 to 12 kW (85% and 92% of the load power injected by the GFe-VSC). MG2 became unstable with the load step at $t = 2$ s. The load returned to 13 kW at $t = 14$ s, and then the system regained its stability.

D. Validation of Design Procedure for Control Parameters

Controllers of MG1 and MG2 for SC20 and SC21 were redesigned following the guidelines introduced in Section V-C yielding SC22 and SC23, respectively. In MG1, the current controller and the PLL of the GFe-VSC were designed to have bandwidths 380 and 7 Hz, respectively. In MG2, the current and voltage controller bandwidths of the GFo-VSC were readjusted to 380 and 40 Hz, respectively. Meanwhile, the bandwidths of PLL and the current controller in GFe-VSC were increased to 380 and 7 Hz, respectively.

Figs. 15(c) and (d) and 16(c) and (d) show the dynamic response of the MGs for SC22 and SC23, respectively, when the load changes were applied as in Fig. 14. In this case, the MGs did not become unstable due to the improved controller design. Figs. 15(a) and 16(a) show the low-frequency eigenvalues for the two MGs at their operating point. The transient responses

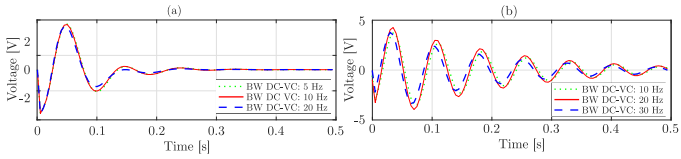

Fig. 17. Response of MG2 (v_{dPLL}) when there is a 3 kW change of the load and the dc-voltage controller has different bandwidths. (a) SC21 with PLL bandwidth of 10 Hz and (b) SC21 with PLL bandwidth of 20 Hz (stability limit).

associated with the pairs of eigenvalues in Figs. 15(a) and 16(a) are depicted in Figs. 15(b) and 16(b). These responses are calculated as $y_i(t) = e^{\lambda_i t}$.

In MG1, the dynamic response of ω_r can be represented as a linear combination of the time characteristics of the dominant eigenvalues 5–8, as the participation matrix suggests in Fig. 5. Also, the time response of v_d can be represented as a linear combination of the time characteristics of eigenvalues 9 and 10. Similarly, in MG2, the responses of the voltage and frequency can be represented as a linear combination of the time characteristics of eigenvalues 6–7 and 4–5, respectively. These eigenvalues are mainly linked with the states of the voltage controller and the droop control, respectively, as shown in Fig. 7.

VII. Discussion

A. Controller Design and Interactions

The analysis of participation factors confirmed that low-frequency modes are affected by the PLL states and, simultaneously, by the mechanical states of the diesel gen-set and the states of the current and voltage controllers. The eigenvalue analysis revealed the PLL design is closely linked with the loading conditions and the design of the voltage and current controllers of the VSCs. In general, slow GFe-VSC current controllers, slow GFo-VSC voltage controllers, and fast GFo-VSC current controllers limit the range of the PLL bandwidth in which the stability is guaranteed. Previous studies also showed that systems may become unstable when the PLL and the dc-voltage controller have similar bandwidths [16], [17]. Therefore, the PLL design is crucial and critical for the stability of an MG.

B. Additional Control Loops

The study did not reveal any relevant interactions between the PLL and the voltage control loop of the SG (excitation and AVR), as it was previously reported in the literature for other types of excitation. The most likely cause is that in these works, a static excitation system was used, while in this one, it is based on alternating current. Also, as reported in the literature, the dc-voltage controller may interact with the PLL and cause instabilities [10], [16], [17]. In order to study this interaction, a standard dc-voltage controller was implemented in the GFe-VSC [7]. Then, the response of v_{dPLL} was checked for MG2, for different designs of the PLL and the dc-voltage controller. Fig. 17 shows the response of MG2 at SC21 with PLL bandwidth of Fig. 17(a) 10 Hz and Fig. 17(b) 20 Hz (close to the stability limit of the PLL). Fig. 17 shows that v_{dPLL} exhibits an oscillation, which appears as a result of the PLL design. When PLL is close to its stability limit, in Fig. 17(b), the oscillation is poorly damped. Also, it can be seen that the design of the dc-voltage controller

TABLE V
STABILITY LIMITS OF PLL BANDWIDTH UNDER DIFFERENT SCENARIOS. "–" MEANS "LIMIT NOT FOUND."

MG	SC	BW_{CC}	PLL	PLL+DSOGI
MG1	SC20	120 Hz	18 Hz	–
MG1	SC8	120 Hz	3 Hz	3 Hz
MG1	SC8	160 Hz	4 Hz	4 Hz
MG1	SC8	250 Hz	8 Hz	10 Hz
MG2	SC21	250 Hz	1 Hz	–
MG2	SC18	160 Hz	13 Hz	13 Hz
MG2	SC18	260 Hz	–	–

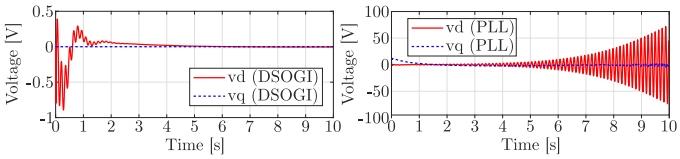

Fig. 18. PCC voltage (in dq) of the nonlinear model of MG1 (SC20), when there is a 1 kW change of the load, with DSOGI-PLL and with PLL.

slightly affects the oscillation. In particular, the amplitude of the oscillation is amplified when the dc-voltage controller and the PLL have the same bandwidths. This result is in agreement with previous studies that show that the interaction between PLL and dc-voltage controller is stronger when they have similar bandwidths [16], [17]. Therefore, it would be of interest to study in detail the cases in which the PLL interacts with other control loops (e.g., the governor of the SG) and also the interaction between dc-voltage controller and the rest of the MG controllers.

C. Advanced PLL Structures

In order to study the effect of advanced synchronization techniques, the dual second-order generalized integrator (DSOGI) was implemented to calculate the positive sequence of the PCC voltage in the studied MGs [6]. For MG1 and MG2, the nonlinear models were used to obtain the stability limits of the DSOGI-PLL bandwidth under different scenarios. Table V shows a comparison of the obtained stability limits of the PLL bandwidth, with and without the additional DSOGI. Both implementations have similar stability limits, although those obtained with the DSOGI were slightly wider. In some scenarios, like in SC20, the MG is stable for all the values of the PLL bandwidth when the DSOGI is used. Fig. 18 (SC20) shows that MG1 remains stable under load changes if a DSOGI-PLL is used, confirming the results presented in Table V. From these results, it can be seen that advanced synchronization techniques may offer extended stability limits, yet they have to be studied in more detail.

VIII. CONCLUSION

In this article, the dynamic interactions between a GFe-VSC with PLL and two types of GFo devices (diesel gen-set and droop-controlled VSC) in MGs have been studied. Detailed small-signal models for the two different GFo cases have been derived analytically first and then participation factor and eigenvalue analyses have been used to study the interactions between PLL and other devices in the MG. All the theoretical developments have been validated experimentally.

The stability studies as well as the proposed design guidelines have been presented in this article to help MG designers understand the interactions between GFe PLL, GFo devices, and other elements in MGs and facilitate the correct configuration of the control system parameters. The experimental results and the results obtained from the small-signal models showed a good match. Small deviations were seen only for the parameter values that made the system operate close to the maximum PLL bandwidth allowed. Finally, the experimental results for the control system configured according to the proposed design guidelines confirmed that the dynamic response of MGs can be significantly improved by following the developed design criteria.

In future, it would be of interest to study the effect of different SG voltage control loops (especially of those with static excitation and fast AVR), the impact of more advanced PLL topologies, as well as the interactions between the dc-voltage controller and other control loops.

APPENDIX

A. State-Space Matrices of the SG

1) State-Space Matrices of the Electromechanical Model: The equations linking DQ stator and rotor flux linkages in an SG with damper windings are [18]

$$v_{sg}^{D} = \frac{d\psi^{D}}{dt} - \omega_r \psi^{Q} - r_a i^{D} \tag{33}$$

$$v_{sg}^{Q} = \frac{d\psi^{Q}}{dt} + \omega_r \psi^{D} - r_a i^{Q} \tag{34}$$

$$v_f = \frac{d\psi_f}{dt} + r_f i_f \tag{35}$$

$$0 = \frac{d\psi_k^{D}}{dt} + r_{kd} i_k^{D} \tag{36}$$

$$0 = \frac{d\psi_k^{Q}}{dt} + r_{kq} i_k^{Q} \tag{37}$$

where the stator and rotor flux linkages are defined as [18]

$$\psi^{D} = -l_d i_{sg}^{D} + l_{afd} i_f + l_{akd} i_k^{D} \tag{38}$$

$$\psi^{Q} = -l_q i_{sg}^{Q} + l_{akq} i_k^{Q} \tag{39}$$

$$\psi_f = l_{ff} i_f + l_{fkd} i_k^{D} - l_{afd} i_{sg}^{D} \tag{40}$$

$$\psi_k^{D} = l_{fkd} i_f + l_{kkd} i_k^{D} - l_{akd} i_{sg}^{D} \tag{41}$$

$$\psi_k^{Q} = l_{kkq} i_k^{Q} - l_{akq} i_Q. \tag{42}$$

The linearization of the previous equations yields the following state-space matrices:

$$A_{EM} = M_R M_L^{-1} + M_\omega \tag{43}$$

$$M_R = \begin{bmatrix} r_a & 0 & 0 & 0 & 0 \\ 0 & -r_f & 0 & 0 & 0 \\ 0 & 0 & -r_{kd} & 0 & 0 \\ 0 & 0 & 0 & r_a & 0 \\ 0 & 0 & 0 & 0 & -r_{kq} \end{bmatrix} \tag{44}$$

$$M_\omega = \begin{bmatrix} 0 & 0\,0\,\Omega_r & 0 \\ 0 & 0\,0\,0 & 0 \\ 0 & 0\,0\,0 & 0 \\ -\Omega_r & 0\,0\,0 & 0 \\ 0 & 0\,0\,0 & 0 \end{bmatrix} \tag{45}$$

where M_L^{-1} is the inverse of M_L, which is derived from (38) to (42) as follows:

$$\begin{bmatrix} \Delta\psi^D \\ \Delta\psi_f \\ \Delta\psi_k^D \\ \Delta\psi^Q \\ \Delta\psi_k^Q \end{bmatrix} = M_L \begin{bmatrix} \Delta i_{sg}^D \\ \Delta i_f \\ \Delta i_k^D \\ \Delta i_{sg}^Q \\ \Delta i_k^Q \end{bmatrix} \tag{46}$$

where

$$M_L^{-1} = \begin{bmatrix} K_{id\_fd} & K_{id\_ff} & K_{id\_fkd} & 0 & 0 \\ K_{if\_fd} & K_{if\_ff} & K_{if\_fkd} & 0 & 0 \\ K_{ikd\_fd} & K_{ikd\_ff} & K_{ikd\_fkd} & 0 & 0 \\ 0 & 0 & 0 & K_{iq\_fq} & K_{iq\_fkq} \\ 0 & 0 & 0 & K_{ikq\_fq} & K_{ikq\_fkq} \end{bmatrix}. \tag{47}$$

The rest of the matrices of the electromagnetic model are

$$B_{EM1} = \begin{bmatrix} 0 \\ 1 \\ 0 \\ 0 \\ 0 \\ 0 \end{bmatrix},\ B_{EM2} = \begin{bmatrix} 1\ 0 \\ 0\ 0 \\ 0\ 0 \\ 0\ 1 \\ 0\ 0 \end{bmatrix},\ B_{EM3} = \begin{bmatrix} 0 \\ \Psi_q \\ 0 \\ 0 \\ -\Psi_d \\ 0 \end{bmatrix} \tag{48}$$

$$C_{EM1} = \begin{bmatrix} (K_{iq\_fq} - K_{id\_fd})\Psi_Q + K_{iq\_fkq}\Psi_k^Q \\ -K_{id\_ff}\Psi_Q \\ -K_{id\_fkd}\Psi_Q \\ (K_{iq\_fq} - K_{id\_fd})\Psi_D - K_{id\_fd}\Psi_f - K_{id\_fkd}\Psi_k^D \\ K_{iq\_fkq}\Psi_D \end{bmatrix}^T \tag{49}$$

$$C_{EM2} = \begin{bmatrix} K_{id\_fd} & K_{id\_ff} & K_{id\_fkd} & 0 & 0 \\ 0 & 0 & 0 & K_{iq\_fq} & K_{iq\_fkq} \end{bmatrix} \tag{50}$$

$$C_{EM3} = \begin{bmatrix} K_{if\_fd} & K_{if\_ff} & K_{if\_fkd} & 0 & 0 \end{bmatrix} \tag{51}$$

where the parameters inside matrices are defined here

$$K_{id\_fd} = \frac{-{l_{fkd}}^2 + l_{ff}l_{kkd}}{K_{id\_f}},\ K_{id\_ff} = \frac{(l_{fkd} - l_{kkd})l_{ad}}{K_{id\_f}} \tag{52}$$

$$K_{id\_fkd} = \frac{(-l_{ff} + l_{fkd})l_{ad}}{K_{id\_f}}, K_{if\_fd} = \frac{(-l_{fkd} + l_{kkd})l_{ad}}{K_{id\_f}} \tag{53}$$

$$K_{if\_ff} = \frac{{l_{ad}}^2 - l_d l_{kkd}}{K_{id\_f}},\ \ K_{if\_fkd} = \frac{-{l_{ad}}^2 + l_d l_{fkd}}{K_{id\_f}} \tag{54}$$

$$K_{ikd\_fd} = \frac{(l_{ff} - l_{fkd})l_{ad}}{K_{id\_f}},\ \ K_{ikd\_ff} = \frac{-{l_{ad}}^2 + l_d l_{fkd}}{K_{id\_f}} \tag{55}$$

$$K_{ikd\_fkd} = \frac{{l_{ad}}^2 - l_d l_{ffd}}{K_{id\_f}} \tag{56}$$

$$K_{id\_f} = {l_{ad}}^2(l_{ff} + l_{kkd} - 2l_{fkd}) + l_d{l_{fkd}}^2 - l_d l_{ff} l_{kkd} \tag{57}$$

$$K_{iq\_f} = {l_{aq}}^2 - l_{kkq}l_q,\ K_{iq\_fq} = \frac{l_{kkq}}{K_{iq\_f}} \tag{58}$$

$$K_{iq\_fkq} = \frac{-l_{aq}}{K_{iq\_f}},\ K_{ikq\_fq} = \frac{l_{aq}}{K_{iq\_f}},\ K_{ikq\_fkq} = \frac{-l_q}{K_{iq\_f}}. \tag{59}$$

2) State-Space Matrices of the Shaft: The matrices that define the linear model of the shaft are

$$B_{S1} = \begin{bmatrix} 1/2H \end{bmatrix},\ \ B_{S2} = \begin{bmatrix} -1/2H \end{bmatrix}. \tag{60}$$

3) State-Space Matrices of the Excitation Model: The following matrices are used in the excitation model:

$$A_E = \begin{bmatrix} -(S_E + K_E)/T_E \end{bmatrix},\ \ B_{E1} = \begin{bmatrix} 1/T_E \end{bmatrix},\ \ C_E = \begin{bmatrix} 1 \end{bmatrix}. \tag{61}$$

4) State-Space Matrices of the Diesel Engine: The model of the diesel engine is linearized around the operating point, yielding the following state-space matrices:

$$A_D = \begin{bmatrix} \frac{-(\sigma + F)}{\tau_m(\sigma + T_m)^2} \end{bmatrix},\ \ B_D = \begin{bmatrix} \frac{1}{\tau_m(\sigma + T_m)} \end{bmatrix}. \tag{62}$$

5) State-Space Matrices of the AVR: The matrices below represent the state-space model of the linearized AVR

$$B_{AVR1} = \begin{bmatrix} 1 \end{bmatrix},\ B_{AVR2} = \begin{bmatrix} \frac{-V_{sg}^D}{\sqrt{{V_{sg}^D}^2 + {V_{sg}^Q}^2}} & \frac{-V_{sg}^Q}{\sqrt{{V_{sg}^D}^2 + {V_{sg}^Q}^2}} \end{bmatrix} \tag{63}$$

$$C_{AVR} = \begin{bmatrix} k_{iAVR} \end{bmatrix},\ \ D_{AVR1} = \begin{bmatrix} k_{pAVR} \end{bmatrix} \tag{64}$$

$$D_{AVR2} = \begin{bmatrix} \frac{-V_{sg}^D k_{pAVR}}{\sqrt{{V_{sg}^D}^2 + {V_{sg}^Q}^2}} & \frac{-V_{sg}^Q k_{pAVR}}{\sqrt{{V_{sg}^D}^2 + {V_{sg}^Q}^2}} \end{bmatrix}. \tag{65}$$

6) State-Space Matrices of the Speed Governor: The matrices below represent the state-space model of the speed governor of the SG

$$B_{Gov1} = \begin{bmatrix} 1 \end{bmatrix},\ B_{Gov2} = \begin{bmatrix} -1 \end{bmatrix},\ C_{Gov} = \begin{bmatrix} k_{iGov} \end{bmatrix} \tag{66}$$

$$D_{Gov1} = \begin{bmatrix} k_{pGov} \end{bmatrix},\ \ D_{Gov2} = \begin{bmatrix} -k_{pGov} \end{bmatrix}. \tag{67}$$

7) State-Space Matrices of the Diesel Gen-Set Model: The auxiliary matrices of the diesel generator aggregated small-signal model are presented as follows:

$$[\Delta x_{SG}] = \left[\Delta\alpha, \Delta\beta, \Delta v_f, \Delta t_m, \Delta\psi_d, \Delta\psi_f, \Delta\psi_{kd}, \Delta\psi_q, \Delta\psi_{kq}, \Delta\omega_r\right]^T \tag{68}$$

$$A_{SG} = \begin{bmatrix} 0 & 0 & 0 & 0 & 0 & 0 \\ 0 & 0 & 0 & 0 & 0 & B_{Gov2} \\ B_E C_{AVR} & 0 & A_E & 0 & B_{E2}C_{EM3} & 0 \\ 0 & B_D C_{Gov} & 0 & A_D & 0 & B_D D_{Gov2} \\ 0 & 0 & B_{EM1}C_E & 0 & A_{EM} & B_{EM3} \\ 0 & 0 & 0 & B_{S1} & B_{S2}C_{EM1} & 0 \end{bmatrix} \tag{69}$$

$$[\Delta u_{SG}] = \left[\Delta v_{sg}^*,\ \Delta\omega_{sg}^*,\ \Delta v_{pcc}^{DQ}\right]^T \tag{70}$$

$$B_{SG1} = \frac{1}{U_B}\left[B_{AVR1},\ 0,\ B_{E1}D_{AVR1},\ 0,\ 0,\ 0\right]^T \tag{71}$$

$$B_{SG2} = \frac{1}{\omega_B}\left[0,\ B_{Gov1},\ 0,\ B_D D_{Gov1},\ 0,\ 0\right]^T \tag{72}$$

$$B_{SG3} = \frac{1}{U_B}\left[B_{AVR2},\ 0,\ B_{E1} D_{AVR2},\ 0,\ B_{EM2},\ 0\right]^T \tag{73}$$

$$C_{SG1} = I_B\left[0,0,0,0,C_{EM2},0\right]^T,\ C_{SG2} = \omega_B\left[0,\ldots,0,1\right]^T. \tag{74}$$

B. State-Space Models of Converters Subsystems

1) LCL Filter Model: The complete small-signal model of the LCL filter can be found in the literature [19]. If the state variables are $x_{LCL} = [\Delta i_i^{dq}\ \Delta v_c^{dq}\ \Delta i_o^{dq}]^T$, then

$$[\dot{x}_{LCL}]_i = A^i_{LCL}[x_{LCL}]_i + B^i_{LCL1}\left[\Delta v_i^{dq}\right]_i + B^i_{LCL2}\left[\Delta v_{pcc}^{dq}\right]_i + B^i_{LCL3}\left[\Delta\omega_{PLL}\right]_i \tag{75}$$

where i denotes the ith converter.

The LCL filter auxiliary matrices are presented as follows:

$$A^i_{LCL} = \begin{bmatrix} \frac{-R_i}{L_i} & \Omega_i & \frac{-1}{L_i} & 0 & 0 & 0 \\ -\Omega_i & \frac{-R_i}{L_i} & 0 & \frac{-1}{L_i} & 0 & 0 \\ \frac{1}{C_d} & 0 & 0 & \Omega_i & \frac{-1}{C_d} & 0 \\ 0 & \frac{1}{C_d} & -\Omega_i & 0 & 0 & \frac{-1}{C_d} \\ 0 & 0 & \frac{1}{L_o} & 0 & \frac{-R_o}{L_o} & \Omega_i \\ 0 & 0 & 0 & \frac{1}{L_o} & -\Omega_i & \frac{-R_o}{L_o} \end{bmatrix}_i \tag{76}$$

$$B^i_{LCL1} = \begin{bmatrix} \frac{1}{L_i} & 0 \\ 0 & \frac{1}{L_i} \\ 0 & 0 \\ 0 & 0 \\ 0 & 0 \\ 0 & 0 \end{bmatrix}_i, B^i_{LCL2} = \begin{bmatrix} 0 & 0 \\ 0 & 0 \\ 0 & 0 \\ 0 & 0 \\ \frac{-1}{L_o} & 0 \\ 0 & \frac{-1}{L_o} \end{bmatrix}_i \tag{77}$$

$$B^i_{LCL3} = \left[I_{iq}, -I_{id}, V_{oq}, -V_{od}, I_{oq}, -I_{od}\right]_i^T. \tag{78}$$

2) Current Controller: A current controller generates the command for the modulation stage of the VSC $(v_i^{*dq})_i$ [19]

$$\left[\Delta\dot{\gamma}^{dq}\right]_i = B^i_{CC1}\left[\Delta i_i^{*dq}\right]_i + B^i_{CC2}[x_{LCL}]_i \tag{79}$$

$$\left[\Delta v_i^{*dq}\right]_i = C^i_{CC}\left[\Delta\gamma^{dq}\right]_i + D^i_{CC1}\left[\Delta i_i^{*dq}\right]_i + D^i_{CC2}[x_{LCL}]_i \tag{80}$$

The current controller is defined by the following space-state matrices

$$B^i_{CC1} = \begin{bmatrix} 1 & 0 \\ 0 & 1 \end{bmatrix}_i, B^i_{CC2}\begin{bmatrix} -1 & 0 & 0 & 0 & 0 & 0 \\ 0 & -1 & 0 & 0 & 0 & 0 \end{bmatrix}_i \tag{81}$$

$$C^i_{CC} = \begin{bmatrix} k_{ic} & 0 \\ 0 & k_{ic} \end{bmatrix}_i,\ D^i_{CC1} = \begin{bmatrix} k_{pc} & 0 \\ 0 & k_{pc} \end{bmatrix}_i \tag{82}$$

$$D^i_{CC2} = \begin{bmatrix} -k_{pc} & -w_n L_i & 0 & 0 & 0 & 0 \\ w_n L_i & -k_{pc} & 0 & 0 & 0 & 0 \end{bmatrix}_i.$$

3) Current Set-Point Calculation: The set-point is calculated in terms of the active and reactive power references. These equations are nonlinear, so they have to be linearized. The nonlinear equations are

$$i^{*d} = \frac{p^* v^d_{pcc} + q^* v^q_{pcc}}{{v^d_{pcc}}^2 + {v^q_{pcc}}^2},\ \ i^{*q} = \frac{-q^* v^d_{pcc} + p^* v^q_{pcc}}{{v^d_{pcc}}^2 + {v^q_{pcc}}^2} \tag{83}$$

while the linearised model is

$$\left[\Delta i_i^{*dq}\right]_i = D^i_{I1}\begin{bmatrix}\Delta p^* \\ \Delta q^*\end{bmatrix}_i + D^i_{I2}\left[\Delta v_{pcc}^{dq}\right]_i \tag{84}$$

with

$$D^i_{I1} = \begin{bmatrix} \frac{V_{bd}}{V_{bd}^2+V_{bq}^2} & \frac{V_{bq}}{V_{bd}^2+V_{bq}^2} \\ \frac{V_{bq}}{V_{bd}^2+V_{bq}^2} & \frac{-V_{bd}}{V_{bd}^2+V_{bq}^2} \end{bmatrix}_i \tag{85}$$

$$D^i_{I2} = \begin{bmatrix} \frac{P(V_{bd}^2+V_{bq}^2)-2V_{bd}(PV_{bd}+QV_{bq})}{(V_{bd}^2+V_{bq}^2)^2} & \frac{Q(V_{bd}^2+V_{bq}^2)-2V_{bq}(PV_{bd}+QV_{bq})}{(V_{bd}^2+V_{bq}^2)^2} \\ \frac{-Q(V_{bd}^2+V_{bq}^2)-2V_{bd}(-QV_{bd}+PV_{bq})}{(V_{bd}^2+V_{bq}^2)^2} & \frac{P(V_{bd}^2+V_{bq}^2)-2V_{bq}(-QV_{bd}+PV_{bq})}{(V_{bd}^2+V_{bq}^2)^2} \end{bmatrix}_i. \tag{86}$$

4) State-Space Matrices of the PLL: The state-space model of the PLL is defined by the matrices as follows:

$$A^i_{PLL} = \begin{bmatrix} A_{PLL_{ee}} & A_{PLL_{ed}} \\ A_{PLL_{de}} & A_{PLL_{dd}} \end{bmatrix}_i = \begin{bmatrix} 0 & k_{ipll} T_{Vd}^{-1} \\ 1 & k_{ppll} T_{Vd}^{-1} \end{bmatrix}_i \tag{87}$$

$$B^i_{PLL1} = \begin{bmatrix} B_{PLL1e} \\ B_{PLL1d} \end{bmatrix}_i = \begin{bmatrix} k_{ipll} T_{Sd}^{-1} \\ k_{ppll} T_{Sd}^{-1} \end{bmatrix}_i \tag{88}$$

$$B^i_{PLL2} = \begin{bmatrix} B_{PLL2e} \\ B_{PLL2d} \end{bmatrix}_i = \begin{bmatrix} 0 \\ -1 \end{bmatrix}_i. \tag{89}$$

5) Voltage Controller: A PI controller is used to control the voltage of the ac capacitor. This controller is modeled as in [19]. The linearized equations are

$$\left[\Delta\dot{\phi}^{dq}\right]_i = B^i_{VC1}\left[\Delta v_c^{*dq}\right]_i + B^i_{VC2}[x_{LCL}]_i \tag{90}$$

$$\left[\Delta i_i^{*dq}\right]_i = C^i_{VC}\left[\Delta\phi^{dq}\right]_i + D^i_{VC1}\left[\Delta v_c^{*dq}\right]_i + D^i_{VC2}[x_{LCL}]_i. \tag{91}$$

The state-space matrices of the voltage controller are

$$B^i_{VC1} = \begin{bmatrix} 1 & 0 \\ 0 & 1 \end{bmatrix}_i,\ B^i_{VC2}\begin{bmatrix} 0 & 0 & -1 & 0 & 0 & 0 \\ 0 & 0 & 0 & -1 & 0 & 0 \end{bmatrix}_i \tag{92}$$

$$C^i_{VC} = \begin{bmatrix} k_{iv} & 0 \\ 0 & k_{iv} \end{bmatrix}_i,\ D^i_{VC1} = \begin{bmatrix} k_{pv} & 0 \\ 0 & k_{pv} \end{bmatrix}_i \tag{93}$$

$$D^i_{VC2} = \begin{bmatrix} 0 & 0 & -k_{pv} & -w_n C_f & 0 & 0 \\ 0 & 0 & w_n C_f & -k_{pv} & 0 & 0 \end{bmatrix}_i. \tag{94}$$

6) Droop Controller: Frequency and voltage droop controllers are implemented together with active and reactive power low-pass filters to obtain the voltage and frequency set-points [19]. Instantaneous active and reactive powers are calculated as follows:

$$p = v_o^d i_o^d + v_o^q i_o^q,\quad q = -v_o^d i_o^q + v_o^q i_o^d. \tag{95}$$

In addition, ω_{nd} and v_{nd} are considered as inputs of the system. Calling $x_{pq} = [\Delta\delta\ \ \Delta\tilde{P}\ \ \Delta\tilde{Q}]$, then

$$\left[\dot{x}_{pq}\right]_i = A^i_P\left[x_{pq}\right]_i + B^i_{P1}\left[x_{LCL}\right]_i + B^i_{PIn}\begin{bmatrix}\Delta\omega_{nd} \\ \Delta v_{nd}^{dq}\end{bmatrix}_i + B^i_{PV}\left[\Delta v_o^{dq}\right]_i \tag{96}$$

$$\left[\Delta\omega_{com}\right]_i = C^i_{P\omega}\left[x_{pq}\right]_i + D^i_{P\omega}\begin{bmatrix}\Delta\omega_{nd} \\ \Delta v_{nd}^{dq}\end{bmatrix}_i \tag{97}$$

$$\left[\Delta v_c^{*dq}\right]_i = C^i_{PV}\left[x_{pq}\right]_i + D^i_{PV}\begin{bmatrix}\Delta\omega_{nd} \\ \Delta v_{nd}^{dq}\end{bmatrix}_i \tag{98}$$

$$A^{GFe} = \begin{bmatrix} A_{PLLee} & A_{PLLed} & 0 & 0 \\ A_{PLLde} & A_{PLLdd} & 0 & 0 \\ 0 & B_{CC1}D_{I2}T_{Vd}^{-1} & 0 & B_{CC2} \\ B_{LCL3}A_{PLLde} & B_{LCL3}A_{PLLdd} + (B_{LCL1}D_{CC1}D_{I2} + B_{LCL2})T_{Vd}^{-1} & B_{LCL1}C_{CC} & A_{LCL} + B_{LCL1}D_{CC2} \end{bmatrix} \tag{109}$$

$$A^{GFo} = \begin{bmatrix} A_P + B_{PV}\begin{bmatrix} T_V^{-1} & 0 \end{bmatrix} & 0 & 0 & B_{P1} \\ B_{VC1}C_{PV} + B_{VC3}\begin{bmatrix} T_V^{-1} & 0 \end{bmatrix} & A_{VC} & 0 & B_{VC2} \\ B_{CC1}D_{VC1}C_{PV} + B_{CC1}D_{VC3}\begin{bmatrix} T_V^{-1} & 0 \end{bmatrix} & B_{CC1}C_{VC} & A_{CC} & B_{CC1}D_{VC2} + B_{CC2} \\ B_{LCL1}D_{CC_1}D_{VC_1}C_{P_V} + B_{LCL3}C_{P\omega} & B_{LCL1}D_{CC1}C_{VC} & B_{LCL1}C_{CC} & A_{LCL} + B_{LCL1}D_{CC1}D_{VC2} \\ +(B_{LCL1}D_{CC1}D_{VC3} + B_{LCL2})\begin{bmatrix} T_V^{-1} & 0 \end{bmatrix} & & & +B_{LCL1}D_{CC2} \end{bmatrix} \tag{114}$$

where

$$A_P^i = \begin{bmatrix} 0 & -m_p & 0 \\ 0 & -\omega_c & 0 \\ 0 & 0 & -\omega_c \end{bmatrix}_i \tag{99}$$

$$B_{P1}^i = \begin{bmatrix} 0\ 0\ 0\ 0\ \omega_c V_{o_d} & \omega_c V_{o_q} \\ 0\ 0\ 0\ 0\ \omega_c V_{o_q} & -\omega_c V_{o_d} \end{bmatrix}_i,\ B_{P\omega}^i = \begin{bmatrix} -1 \\ 0 \\ 0 \end{bmatrix}_i \tag{100}$$

$$B_{PIn}^i = \begin{bmatrix} 1\ 0\ 0 \\ 0\ 0\ 0 \\ 0\ 0\ 0 \end{bmatrix}_i,\ B_{PV}^i = \begin{bmatrix} 0 & 0 \\ \omega_c I_{o_d} & \omega_c I_{o_q} \\ -\omega_c I_{o_q} & \omega_c I_{o_d} \end{bmatrix}_i \tag{101}$$

$$C_{P\omega}^i = \begin{bmatrix} 0 & -m_p & 0 \end{bmatrix}_i,\ C_{PV}^i = \begin{bmatrix} 0\ 0 & 0 \\ 0\ 0 & -n_q \end{bmatrix}_i \tag{102}$$

$$D_{P\omega}^i = \begin{bmatrix} 1 \end{bmatrix}_i,\ D_{PV}^i = \begin{bmatrix} 0\ 0 \\ 0\ 1 \end{bmatrix}_i. \tag{103}$$

7) State-Space Matrices for Reference Frame Transformations: The following matrices are used for transformations between reference frames:

$$\begin{bmatrix} \Delta i_{o_{DQ}} \end{bmatrix}_i = T_S^i \begin{bmatrix} i_{o_{dq}} \end{bmatrix}_i + T_C^i \begin{bmatrix} \Delta\delta \end{bmatrix}_i \tag{104}$$

$$T_S^i = \begin{bmatrix} \cos\delta_0 & -\sin\delta_0 \\ \sin\delta_0 & \cos\delta_0 \end{bmatrix}_i \tag{105}$$

$$T_C^i = \begin{bmatrix} -I_{od}\sin\delta_0 - I_{oq}\cos\delta_0 \\ I_{od}\cos\delta_0 - I_{oq}\sin\delta_0 \end{bmatrix}_i \tag{106}$$

$$\begin{bmatrix} \Delta v_{b_{dq}} \end{bmatrix}_i = T_S^{-1i} \begin{bmatrix} v_{b_{DQ}} \end{bmatrix}_i + T_V^{-1i} \begin{bmatrix} \Delta\delta \end{bmatrix}_i \tag{107}$$

$$T_V^{-1i} = \begin{bmatrix} -V_{bd}\sin\delta_0 + V_{bq}\cos\delta_0 \\ -V_{bd}\cos\delta_0 - V_{bq}\sin\delta_0 \end{bmatrix}_i \tag{108}$$

where δ_0 has been used instead of Δ to avoid confusion with the incremental operator "Δ."

Equation (109) shown at the top of this page.

C. State-Space Matrices of the GFe-VSC

The matrices used in the GFe-VSC model are

$$B_{PQ}^{GFe} = \begin{bmatrix} 0,\ 0,\ B_{CC1}D_{I1},\ B_{LCL1}D_{CC1}D_{I1} \end{bmatrix}^T \tag{110}$$

$$B_V^{GFe} = \begin{bmatrix} B_{PLL1e} \\ B_{PLL1d} \\ B_{CC1}D_{I2}T_S^{-1} \\ (B_{LCL1}D_{CC1}D_{I2} + B_{LCL2})T_S^{-1} + B_{LCL3}B_{PLL1d} \end{bmatrix} \tag{111}$$

$$B_\omega^{GFe} = \begin{bmatrix} B_{PLL2e},\ B_{PLL_{PLL2d}},\ 0,\ 0 \end{bmatrix}^T \tag{112}$$

$$C^{GFe} = \begin{bmatrix} 0\ T_C\ 0\ T_S \end{bmatrix}. \tag{113}$$

Equation (114) shown at the top of this page.

D. State-Space Matrices of the Droop-Controlled Converter

The matrices of the GFo-VSC are

$$B_{In}^{GFo} = \begin{bmatrix} B_{PIn} \\ B_{VC1}\begin{bmatrix} 0\ D_{PV} \end{bmatrix} \\ B_{CC1}D_{VC1}\begin{bmatrix} 0\ D_{PV} \end{bmatrix} \\ \begin{bmatrix} B_{LCL3}D_{P\omega}\ B_{LCL1}D_{CC1}D_{VC1}D_{PV} \end{bmatrix} \end{bmatrix} \tag{115}$$

$$B_V^{GFo} = \begin{bmatrix} B_{PV}T_s^{-1} \\ B_{VC3}T_s^{-1} \\ B_{CC1}D_{VC3}T_s^{-1} \\ (B_{LCL2} + B_{LCL1}D_{CC1}D_{VC3})T_s^{-1} \end{bmatrix} \tag{116}$$

$$B_{\omega com}^{GFo} = \begin{bmatrix} B_{P\omega} \\ [0] \end{bmatrix},\ C_I^{GFo} = \begin{bmatrix} \begin{bmatrix} T_C\ 0 \end{bmatrix}\ [0]\ \begin{bmatrix} 0\ T_C \end{bmatrix} \end{bmatrix} \tag{117}$$

$$C_\omega^{GFo} = \begin{bmatrix} C_{P\omega}\ 0 \end{bmatrix},\ D_\omega^{GFo} = \begin{bmatrix} D_{P\omega}\ 0 \end{bmatrix}. \tag{118}$$

E. State-Space Matrices of Linear $R-L$ Load

The state-space matrices of the load are

$$A_L = \begin{bmatrix} \frac{-R_l}{L_l} & \Omega_{sg} \\ -\Omega_{sg} & \frac{-R_l}{L_l} \end{bmatrix},\ B_{L1} = \begin{bmatrix} \frac{1}{L_l} & 0 \\ 0 & \frac{1}{L_l} \end{bmatrix} \tag{119}$$

$$B_{L2} = \begin{bmatrix} I_L^Q \\ -I_L^D \end{bmatrix},\ C_L = \begin{bmatrix} 1\ 0 \\ 0\ 1 \end{bmatrix}. \tag{120}$$

F. State-Space Matrices of the Auxiliary Resistor

The state-space matrices of the auxiliary R are

$$D_{R1} = \begin{bmatrix} \frac{1}{R_x} & 0 \\ 0 & \frac{1}{R_x} \end{bmatrix},\ D_{R2} = \begin{bmatrix} \frac{-1}{R_x} & 0 \\ 0 & \frac{-1}{R_x} \end{bmatrix}. \tag{121}$$

REFERENCES

[1] D. P. Morán-Río, J. Roldán-Pérez, M. Prodanovic, and A. Garcıa-Cerrada, "Influence of PLL parameters on small-signal stability of microgrids with synchronous generators," in *Proc. IEEE Energy Convers. Congr. Expo.*, 2020, pp. 2451–2458.

[2] N. Hatziargyriou, *Microgrids: Architectures and Control*. Hoboken, NJ, USA: Wiley, 2014.

[3] A. Ogunjuyigbe, T. Ayodele, and O. Akinola, "Optimal allocation and sizing of PV/wind/split-diesel/battery hybrid energy system for minimizing life cycle cost, carbon emission and dump energy of remote residential building," *Appl. Energy*, vol. 171, pp. 153–171, 2016.

[4] D. E. Olivares *et al.*, "Trends in microgrid control," *IEEE Trans. Smart Grid*, vol. 5, no. 4, pp. 1905–1919, Jul. 2014.

[5] M. Farrokhabadi *et al.*, "Microgrid stability definitions, analysis, and modeling," IEEE PES Task Force on Microgrid Stability Analysis and Modeling, Tech. Rep. PES-TR66, Apr. 2018.

[6] R. Teodorescu, M. Liserre, and P. Rodriguez, *Grid Converters for Photovoltaic and Window Power* System. Hoboken, NJ, USA: Wiley, 2011.

[7] A. Yazdani and R. Iravani, *Voltage-Sourced Converters in Power. System.: Modeling, Control, and Applications*. Hoboken, NJ, USA: Wiley, 2010.

[8] B. Wen, D. Boroyevich, R. Burgos, P. Mattavelli, and Z. Shen, "Analysis of D-Q small-signal impedance of grid-tied inverters," *IEEE Trans. Power Electron.*, vol. 31, no. 1, pp. 675–687, Jan. 2016.

[9] J. Z. Zhou, H. Ding, S. Fan, Y. Zhang, and A. M. Gole, "Impact of short-circuit ratio and phase-locked-loop parameters on the small-signal behavior of a VSC-HVDC converter," *IEEE Trans. Power Del.*, vol. 29, no. 5, pp. 2287–2296, Oct. 2014.

[10] L. Harnefors, X. Wang, A. G. Yepes, and F. Blaabjerg, "Passivity-based stability assessment of grid-connected VSCs-An overview," *IEEE Trans. Emerg. Sel. Topics Power Electron.*, vol. 4, no. 1, pp. 116–125, Mar. 2016.

[11] F. Katiraei, M. R. Iravani, and P. W. Lehn, "Small-signal dynamic model of a micro-grid including conventional and electronically interfaced distributed resources," *IET Gener. Transmiss. Distrib.*, vol. 1, no. 3, pp. 369–378, 2007.

[12] F. Katiraei, "Dynamic analysis and control of distributed energy resources in a micro-grid," Ph.D. dissertation, Dept. Elect. Comput. Eng., Univ. Toronto, Toronto, ON, Canada, 2005.

[13] X. Tang, W. Deng, and Z. Qi, "Investigation of the dynamic stability of microgrid," *IEEE Trans. Power Syst.*, vol. 29, no. 2, pp. 698–706, Mar. 2014.

[14] Y. Lin, B. Johnson, V. Gevorgian, V. Purba, and S. Dhople, "Stability assessment of a system comprising a single machine and inverter with scalable ratings," in *Proc. North Amer. Power Symp.*, 2017, pp. 1–6.

[15] J. Guo, T. Chen, B. Chaudhuri, and S. Y. R. Hui, "Stability of isolated microgrids with renewable generation and smart loads," *IEEE Trans. Sustain. Environ.*, vol. 11, no. 4, pp. 2845–2854, Oct. 2020.

[16] Y. Huang, X. Yuan, J. Hu, and P. Zhou, "Modeling of VSC connected to weak grid for stability analysis of DC-link voltage control," *IEEE Trans. Emerg. Sel. Topics Power Electron.*, vol. 3, no. 4, pp. 1193–1204, Dec. 2015.

[17] D. Wang, L. Liang, L. Shi, J. Hu, and Y. Hou, "Analysis of modal resonance between PLL and DC-link voltage control in weak-grid tied VSCs," *IEEE Trans. Power Syst.*, vol. 34, no. 2, pp. 1127–1138, Mar. 2019.

[18] P. Kundur, *Power System Stability and Control*. New York, NY, USA: McGraw-Hill, 1994.

[19] N. Pogaku, M. Prodanovic, and T. C. Green, "Modeling, analysis and testing of autonomous operation of an inverter-based microgrid," *IEEE Trans. Power Electron.*, vol. 22, no. 2, pp. 613–625, Mar. 2007.

[20] J. V. Knudsen, "Modeling, control, and optimization for diesel-driven generator sets," Ph.D. dissertation, Dept. Electron. Syst., Aalborg Univ., Aalborg, Denmark, 2017.

[21] I. Boldea, *Synchronous Generators*. New York, NY, USA: Taylor & Francis Group, 2006.

[22] P. C. Krause, O. Wasynczuk, and S. D. Sudhoff, *Analysis of Electric Machinery and Drive Systems*, 2nd ed. Hoboken, NJ, USA: Wiley, Feb. 2002.

[23] *IEEE421.5–2016: Recommended Practice for Excitation System Models for Power System Stability Studies*, IEEE Standard 421.5-2016 (Revision of IEEE Standard 421.5-2005), pp. 1–207, Aug. 2016.

[24] A. Rodrıguez-Cabero, M. Prodanovic, and J. Roldán-Perez, "Analysis of dynamic properties of VSCs connected to weak grids including the effects of dead time and time delays," *IEEE Trans. Sustain. Energy*, vol. 10, no. 3, pp. 1066–1075, Jul. 2019.

[25] A. Monti, F. Milano, E. Bompard, and X. Guillaud, *Converter-Based Dynamics and Control of Modern Power Systems*. San Diego, CA, USA: Academic, 2020.

[26] L. Harnefors, "Implementation of resonant controllers and filters in fixed-point arithmetic," *IEEE Trans. Ind. Electron.*, vol. 56, no. 4,

[27] "Regulations for grid connection - EnergiNet," Accessed: Mar. 25, 2021. [Online]. Available: https://en.energinet.dk/ Electricity/Rules-and-Regulations/Regulations-for-grid-connection

[28] "Simulink control design toolbox," Accessed: Mar. 31, 2021. [Online]. Available: https://es.mathworks.com/products/ simcontrol.html

[29] M. Prodanovic, A. Rodríguez-Cabero, M. Jiménez-Carrizosa, and J. Roldán-Pérez, "A rapid prototyping environment for DC and AC microgrids: Smart Energy Integration Lab (SEIL)," in *Proc. IEEE 2nd Int. Conf. DC Microgrids*, 2017, pp. 421–427.

[30] F. Huerta, J. K. Gruber, M. Prodanovic, and P. Matatagui, "Power-hardware-in-the-loop test beds: Evaluation tools for grid integration of distributed energy resources," *IEEE Ind. Appl. Mag.*, vol. 22, no. 2, pp. 18–26, Mar./Apr. 2016.

[31] P. Vorobev, P. H. Huang, M. A. Hosani, J. L. Kirtley, and K. Turitsyn, "High-fidelity model order reduction for microgrids stability assessment," *IEEE Trans. Power Syst.*, vol. 33, no. 1, pp. 874–887, Jan. 2018.

Diana Patricia Morán-Río received the B.Sc. degree in electrical engineering and the M.Sc. degree in industrial engineering from the University of Valladolid, Valladolid, Spain, in 2014 and 2016, respectively.

From 2016 to 2018, she was a Power-lines Project Engineer for transport and distribution companies in Spain. Since 2018, she has been with Electrical Systems Unit, IMDEA Energy Institute, Madrid, Spain. In 2021, she was a visiting Ph.D. student with the Center of Energy, Austrian Institute of Tecnology (AIT), Vienna, Austria. Her research interests include integration of renewable energies and electrical storage, modeling of electrical networks, microgrids, and secondary control.

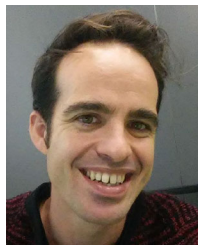

Javier Roldán-Pérez (Member, IEEE) received the B.S. degree in industrial engineering, the M.S. degrees in electronics and control systems, and in system modeling, and the Ph.D. degree in power electronics, all from Comillas Pontifical University, Madrid, Spain, in 2009, 2010, 2011, and 2015, respectively.

From 2010 to 2015, he was with Institute for Research in Technology (IIT), Comillas University, Madrid, Spain. In 2014, he was a visiting Ph.D. student with the Department of Energy Technology, Aalborg University, Denmark. From 2015 to 2016. He was with Electric and Control Systems Department, Norvento Energía Distribuida. Since September 2016, he has been with Electrical Systems Unit, IMDEA Energy Institute, Madrid, Spain. In 2018, he did a research stay at SINTEF Energy Research, Trondheim. His research interests include the integration of renewable energies, microgrids, and power electronics applications.

Milan Prodanovic (Member, IEEE) received the B.Sc. degree in electrical engineering from the University of Belgrade, Belgrade, Serbia, in 1996, and the Ph.D. degree in electric and electronic engineering from Imperial College, London, U.K., in 2004.

From 1997 to 1999, he was with GVS Engineering Company, Serbia, developing UPS systems. From 1999 to 2010, he was a Research Associate in Electrical and Electronic Engineering with Imperial College. He is currently a Senior Researcher and the Head of Electrical Systems Unit, Institute IMDEA Energy, Madrid, Spain. He has authored a number of highly cited articles and is the holder of three patents. His research interests include design and control of power electronics interfaces for distributed generation, microgrids stability and control, and active management of distribution networks.

Aurelio Garcia-Cerrada (Senior Member, IEEE) received the M.Sc. degree from the Universidad Politécnica de Madrid, Madrid, Spain, in 1986, and the Ph.D. degree from the University of Birmingham, Birmingham, U.K., in 1991.

He is currently a Professor with the Department of Electronics, Control Engineering and Communications, Institute for Research in Technology (IIT), Universidad Pontificia Comillas, Madrid, Spain. His research interests include power electronics and its applications to electric energy systems.

Dr. García-Cerrada is a member of the IEEE and the IET.